A New Particle Filter for Radar Target Tracking and Its Application to MIMO-OFDM ISAC

Shixiong Wang, Wei Dai, and Geoffrey Ye Li, *Fellow, IEEE*

***Abstract*—Target tracking using multi-input multi-output (MIMO) pulse-Doppler radars faces three long-standing obstacles: a) the absence of reliable likelihood models for raw radar data; b) the computational and statistical complications that arise when nuisance parameters (e.g., complex path gains) are augmented into state vectors; and c) the prohibitive computational burden of extracting noisy measurements of range, Doppler, and angles from snapshots. Motivated by an optimization-centric interpretation of Bayes' rule, this article addresses these challenges by proposing a new particle filtering framework that evaluates each hypothesized state using a tailored cost function, rather than relying on an explicit likelihood relation. In addition, we study the integration of the proposed particle filter into MIMO orthogonal frequency-division multiplexing (OFDM) systems, aiming to equip modern communication infrastructure with integrated sensing and communications (ISAC) capabilities. Experiments suggest that the proposed particle filter achieves high tracking performance and computational efficiency in MIMO-OFDM ISAC systems, particularly when wide bandwidth, extended on-target time, and large antenna aperture are utilized.**

***Index Terms*—Particle Filter, Gibbs Posterior, Target Tracking, ISAC, Pulsed Radar, Continuous-Wave Radar, MIMO-OFDM Waveform, Pulse-Doppler Processing.**

I. Introduction

In emerging wireless systems, integrated sensing and communications (ISAC) has been envisioned as a promising solution for enabling both communication and sensing functions on a common hardware platform, leveraging shared resources in power, time, space, and frequency, such as transmit and receive antennas, radio frequency chains, digital signal processing units, and transmit waveforms [1], [2]. This integration can reduce hardware volume, improve resource efficiency, and provide mutual benefits between sensing and communications [3], [4]. Among many sensing aspects (e.g., detection, measuring, tracking, and imaging [5]), target tracking is fundamental and plays a critical role in a broad range of ISAC applications, such as sensing-assisted communications [3] and intelligent transportation [6]. This article is concerned with target tracking problems in ISAC. Particularly, the multi-input multi-output orthogonal frequency-division multiplexing (MIMO-OFDM) systems are investigated for three reasons. First, MIMO technology enables spatial and waveform diversity to enhance communication performance in terms of throughput and reliability [7]–[9], as well as radar sensing performance in terms of angle resolution and spatial interference suppression [10]–[12]. Second, OFDM techniques allow frequency-domain signal processing using fast Fourier transform (FFT) if the duration of the cyclic prefix is sufficient to cover all round-trip target delays [13, p. 19], [14], which brings significant computational benefits to real-world radar operations [15], [16], [17, Eqs. (62)-(63)], especially compared to time-domain integration-based matched filtering for ranging [18], [19]. Third, modern mature wireless communication systems are built upon MIMO-OFDM, such as 4G LTE, 5G NR, Wi-Fi 5/6/6E/7, and even upcoming 6G schemes; the adoption of MIMO-OFDM in 6G has been confirmed by the 3GPP RAN1 Committee in August 2025. Therefore, it is natural to equip these widespread systems with sensing capabilities without requiring large-scale infrastructure modification and software upgradation [13], [15]. Research on MIMO ISAC, OFDM ISAC, and MIMO-OFDM ISAC is flourishing. Remarkable progress in this and related areas includes the following: 1) information-theoretic analyses of systematic and methodological performances [20]–[23]; 2) signal processing methods in target detection and parameter estimation [16], [24]–[26], waveform design [14], [27], [28], beamforming and precoding [29], [30], and pulse shaping and modulation [31], [32]; 3) and practical developments of real-world systems [33]. Target tracking for MIMO-OFDM ISAC systems is also reported, although sparsely, such as [34], where only angles are tracked.

The target tracking problem for a single object can be formulated as [35], [36]

$$\begin{cases} \mathbf{x}_k &= \boldsymbol{f}_k(\mathbf{x}_{k-1}, \mathbf{w}_{k-1}) \\ \mathbf{y}_k &= \boldsymbol{h}_k(\mathbf{x}_k, \mathbf{v}_k), \end{cases} \tag{1}$$

where $k = 0, 1, 2, \ldots$ denotes the discrete time index, $\mathbf{x}_k \in \mathbb{R}^{d_x}$ the target state vector, $\mathbf{y}_k \in \mathbb{R}^{d_y}$ (or $\mathbf{y}_k \in \mathbb{C}^{d_y}$) the measurement vector, $\boldsymbol{f}_k(\cdot,\cdot)$ the state transition function, $\mathbf{w}_k \in \mathbb{R}^{d_w}$ the process noise vector, $\boldsymbol{h}_k(\cdot,\cdot)$ the state measurement function, and $\mathbf{v}_k \in \mathbb{R}^{d_v}$ (or $\mathbf{v}_k \in \mathbb{C}^{d_v}$) the measurement noise vector. Mathematically, a target tracking problem is stated as using the system model (1) and the measurement history $\mathcal{Y}_k \coloneqq \{\mathbf{y}_0, \mathbf{y}_1, \ldots, \mathbf{y}_k\}$, up to and including time k, to infer the unknown target state $\mathbf{x}_k$. Depending on whether the system is linear or nonlinear, state estimation approaches, such as Kalman or particle filtering [37]–[39], serve as the inference engine. The state vector $\mathbf{x}_k$, as per specific applications, can consist of different variables. On the one hand, in Cartesian coordinates, $\mathbf{x}_k$ can denote positions, velocities, and accelerations of the target of interest (ToI) in two- or three-dimensional spaces [35]. On the other hand, in polar coordinates, $\mathbf{x}_k$ can include range, radial speed (or Doppler frequency shift), angles

S. Wang is with the School of Mathematics and Statistics, Xi'an Jiaotong University, Xi'an 710049, China (E-mail: s.wang@xjtu.edu.cn; s.wang@u.nus.edu). W. Dai and G. Y. Li are with the Department of Electrical and Electronic Engineering, Imperial College London, London SW7 2AZ, United Kingdom (E-mails: wei.dai1@imperial.ac.uk; geoffrey.li@imperial.ac.uk). (*Corresponding Author: S. Wang.*)

(e.g., elevation, azimuth), and angular speeds of the ToI in the radar's view field [40], [41]. At times, statistical signal processing methods mandate $\mathbf{x}_k$ to contain some nuisance parameters, for example, the turning rate in a coordinated-turn maneuvering model [35], the model index in a multi-model tracking system [42], or the real and imaginary components of complex path gains [34], [36], [40], [41]. According to the level of radar signal processing, the following two cases for the measurement vector $\mathbf{y}_k$ are standard:

- *Information-Level Tracking*: In this scheme, $\mathbf{y}_k \in \mathbb{R}^{d_y}$ denotes the radar's measurements of range, radial velocity, and angle(s) that are to be assimilated by the target's motion mechanism (1); see, e.g., [5, Chap. 7]. At times, $\mathbf{y}_k \in \mathbb{R}^{d_y}$ can also denote the unfiltered positions and velocities of the ToI, calculated using raw range-Doppler-angle measurements [43], [44, p. 8]. This is the most common way in real-world radar target tracking due to its simplicity in operation. When detection is jointly considered, this paradigm is widely referred to as *detect-then-track* in the literature [45].
- *Signal-Level Tracking*: In this scheme, $\mathbf{y}_k \in \mathbb{C}^{d_y}$ denotes the radar's base-band raw in-phase/quadrature (I/Q) snapshots [36], [40], [41], [46]. Note that within a target tracking period k, a radar can collect several snapshots in fast and slow times; see [5, Sec. 1.5.1]. In this case, the measurement model $\mathbf{y}_k = \boldsymbol{h}_k(\mathbf{x}_k, \mathbf{v}_k)$ is severely nonlinear in $\mathbf{x}_k$,[1] so particle filtering is chosen over Kalman filtering and its variants, such as extended and unscented Kalman filtering, for higher tracking accuracy; see, e.g., [34, Figs. 4-5], [36], [40], [41]. When detection is jointly considered, this paradigm is known as *track-before-detect*, which outperforms detect-then-track in the low signal-to-noise ratio (SNR) regimes [47], [48].

However, three drawbacks of the existing schemes for radar target tracking have to be outlined:

- In information-level tracking, at each time k, obtaining measurements $\boldsymbol{y}_k$ and calibrating their uncertainty quantification parameters (i.e., distribution type, mean, covariance, and other statistics of $\mathbf{v}_k$) are computationally prohibitive, especially when advanced optimization techniques, such as compressed sensing and tensor decomposition, are utilized; see [25], [26], [49, Table II]. Even for matched-filter-based methods that are considered computationally efficient [16], searching for the peaks of the filter outputs in a validation gate is time-consuming as well. The computational burden further increases when particle filtering is afterward employed to link these measurements $\boldsymbol{y}_k$ with the tracking model (1). This issue motivates the methodological shift from information-level tracking to signal-level tracking.
- In signal-level tracking, when raw snapshots $\boldsymbol{y}_k$ are obtained, the next key step is to calculate the likelihoods $q(\boldsymbol{y}_k|\boldsymbol{x}_k)$ of hypothesized states $\boldsymbol{x}_k$; note that the likelihood function $q(\boldsymbol{y}_k|\boldsymbol{x}_k)$ is induced by a nonlinear measurement model $\mathbf{y}_k = \boldsymbol{h}_k(\mathbf{x}_k, \mathbf{v}_k)$. The challenge is that the nonlinear measurement model $\mathbf{y}_k = \boldsymbol{h}_k(\mathbf{x}_k, \mathbf{v}_k)$ is unknown (or uncertain) in practice, so is the probabilistic model $q(\boldsymbol{y}_k|\boldsymbol{x}_k)$, because the information about environmental scatterers (including targets of no interest) and channel noises is lacking. Assuming inexact distribution families or statistics for $q(\boldsymbol{y}_k|\boldsymbol{x}_k)$ cannot offer trustworthy likelihood information.
- To handle unknown parameters involved in the state transition and measurement mechanisms, we usually need to include the nuisance parameters into the state vector $\mathbf{x}_k$, e.g., the turning rate of the coordinated turn model [35], the real and imaginary components of the complex path gain due to the ToI [40], [41]. However, this operation imposes nontrivial complications because the statistical and computational efficiency of particle filters significantly deteriorate when the dimension d_x of the state vector $\mathbf{x}_k$ increases [50], [51]. Even though the Rao-Blackwellized (i.e., marginalized) particle filtering [52], [53] has the potential to mitigate such complications, it remains inadequate for tracking rapidly jumping nuisance parameters if an accurate state-transition model for these parameters is not available. For example, complex path gains can change abruptly across consecutive tracking periods k for fast-fading channels, so the usual first-order Gauss–Markov models (e.g., random walk and constant-velocity models) are not appropriate; see the experiment section for a specific discussion.

To address the above issues of radar target tracking, this article proposes a new particle filtering framework for signal-level target tracking (PF-SLTR), by leveraging the optimization-centric interpretation of Bayes' rule, i.e., the Gibbs posterior [54]–[56]. The advantages of this new framework are threefold:

- We do not require an operationally separate, and computationally expensive, phase to obtain raw radar measurements (e.g., range, Doppler, angles) and calibrate their uncertainty quantification.
- We do not mandate the knowledge of the probabilistic model $q(\boldsymbol{y}_k|\boldsymbol{x}_k)$ to calculate $\boldsymbol{y}_k$-data evidence (i.e., likelihoods) of particles (i.e., hypothesized state values).
- We do not augment the parameters of the complex path gain, due to the ToI, into the state vector.

Technically, the pivotal yet challenging step is to devise an efficient cost function $\rho(\boldsymbol{y}_k, \boldsymbol{x}_k)$ to quantify the $\boldsymbol{y}_k$-data evidence of a hypothesized state $\boldsymbol{x}_k$, which requires problem-specific investigation for signal-level target tracking using MIMO pulse-Doppler radar. Existing general principles and methodologies in applied statistics and machine learning are not directly applicable since the design of ρ is domain-specific and there is no one-size-fits-all solution; cf., e.g., [54]–[58].

Moreover, we adapt the proposed PF-SLTR to MIMO-OFDM ISAC systems, where MIMO-OFDM communication waveforms are reused for high-accuracy target tracking. Radar signal processing for target tracking in both the time domain and the frequency domain is investigated, corresponding to the pulsed radar scheme [59] and the continuous-wave radar scheme [13], [14], respectively.

In summary, the contributions of this article can be outlined

[1]For example, see (2)-(6), where the measurement function is severely nonlinear in ToI's state parameters $(\tau_0, \nu_0, \theta_0)$.

as follows: 1) A new particle filtering framework for signal-level target tracking is studied, which frees practitioners from obtaining raw range-Doppler-angle measurements, specifying the exact likelihood model, and augmenting path gain parameters into the state vector; 2) The usage of the proposed PF-SLTR in MIMO-OFDM ISAC systems is investigated, by designing waveform structures and signal processing chains.

Notations: Let $\mathbb{R}^d$ and $\mathbb{C}^d$ denote the d-dimensional spaces of real and complex numbers, respectively. We use lowercase letters for vectors (e.g., $\boldsymbol{x}$) and uppercase ones for matrices (e.g., $\boldsymbol{X}$), both in boldface; scalars are not boldfaced. Random quantities are written in Roman fonts (e.g., x, $\mathbf{X}$), while deterministic ones are in italic fonts (e.g., x, $\boldsymbol{X}$). Let $\langle x \rangle$ denote the rounding operation of real number x to the nearest integer, and $[N] \coloneqq \{0, 1, 2, \ldots, N-1\}$ the running index set starting from zero for integer N. Let $\boldsymbol{I}_d$ denote the d-dimensional identity matrix, and $\boldsymbol{X}^{\mathsf{T}}$ and $\boldsymbol{X}^{\mathsf{H}}$ the transpose and conjugate transpose of matrix $\boldsymbol{X}$, respectively.

II. Measurement Model and Problem Statements

A. Measurement Model of Signal-Level Target Tracking

In this section, we review the MIMO multi-carrier pulse-Doppler radar model that is suitable for various transmit waveforms, including reused MIMO-OFDM communication waveforms. For conciseness of presentation and without loss of generality, this article specifically investigates a two-dimensional planar target tracking problem so that only one direction-of-arrival (DoA) angle for each target is to be examined. We consider a mono-static ISAC station that is

- Located at the origin $[0, 0]$ and staying unmoving.
- Operating with center frequency f_c, wavelength $\lambda \coloneqq C/f_c$, bandwidth B, sampling time period $T_s \coloneqq 1/B$, and per-antenna power budget P_t; C is the light speed.
- Equipped with a transmit antenna array that includes N_t collocated omnidirectional elements; the transmit steering vector is $\boldsymbol{a}(\theta)$ in direction θ, which is determined by the array geometry.
- Equipped with a receive antenna array that includes N_r collocated omnidirectional elements; the receive steering vector is $\boldsymbol{b}(\theta)$ in direction θ. The receive array and transmit array can operate in either the time-division duplex mode (cf. pulsed radars) or the full-duplex mode (cf. continuous-wave radars with pulse-Doppler processing).
- Configured with target tracking period T_t, i.e., the time interval between $k-1$ and k in (1).

The waveform structures in terms of radar sensing, as illustrated in Fig. 1, are specified as follows.

- Each target tracking period T_t includes one coherent processing interval (CPI) T_i, within which the motion parameters of the ToI remain unchanged and can be resolved. Note that $T_i \le T_t$.
- Each CPI constitutes N_p pulses (i.e., N_p slow times) and each pulse has a time duration T_p. Hence, the number of snapshots within a pulse is $L_{\text{ss}} \coloneqq \langle T_p/T_s \rangle$.
- The pulse repetition interval (PRI) is T_r, and therefore, the pulse repetition frequency (PRF) is $f_r \coloneqq 1/T_r$. Note that $T_p \le T_r \le T_i \le T_t$.
- Each PRI consists of L sampling points, so $T_r = LT_s$. The set $[L]$ defines L fast-time range bins; NB: $L_{\text{ss}} \le L$.

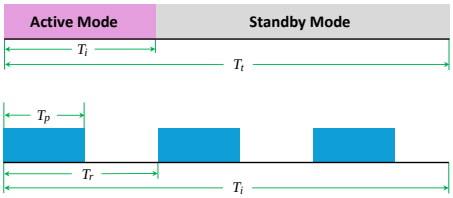


Fig. 1. The time structure of a radar waveform. In the active mode, wireless signals are used for target tracking, while in the standby mode, no tracking task is performed. For illustration, three pulses are shown within one CPI T_i. When $T_r > T_p$ (usually $T_r \gg T_p$), the pulsed radar scheme applies; if $T_r = T_p$, the continuous-wave radar scheme applies. For both schemes, pulse-Doppler signal processing pipelines hold [5], [14].

The above pulse-Doppler radar configurations imply that

- We have the CPI $T_i = N_p T_r$.
- The resolutions of round-trip delay and Doppler frequency are $1/B$ and $1/T_i$, respectively.
- The inter-pulse silent time is $T_r - T_p$.
- In time-division duplex mode, the maximum detectable round-trip delay is $\tau_{\text{max-d}} \coloneqq T_r - T_p$, and the minimum detectable round-trip delay is $\tau_{\text{min-d}} \coloneqq T_p$. In full-duplex mode, $\tau_{\text{max-d}} \coloneqq T_r$ and $\tau_{\text{min-d}} \coloneqq 0$. As a result, the maximum and minimum detectable distances are $R_{\text{max-d}} \coloneqq C\tau_{\text{max-d}}/2$ and $R_{\text{min-d}} \coloneqq C\tau_{\text{min-d}}/2$, respectively.
- The minimum and maximum unambiguous Doppler frequency shifts are $\nu_{\text{min-ua}} \coloneqq -f_r/2$ and $\nu_{\text{max-ua}} \coloneqq f_r/2$, respectively.

In addition, suppose that the ToI within the tracking time period k is characterized by

- The true round-trip delay τ_0, and hence, the true range $R_0 \coloneqq C\tau_0/2$. (Note that $R_{\text{min-d}} \le R_0 \le R_{\text{max-d}}$.)
- The true Doppler frequency shift ν_0, and therefore, the true radial speed $v_0 \coloneqq \nu_0\lambda/2$. (Note that $\nu_{\text{min-ua}} \le \nu_0 \le \nu_{\text{max-ua}}$.)
- The true DoA θ_0 relative to the array boresight. (The transmit array and receive array are supposed to have the same DoA θ_0 for the ToI.)

With the above system settings, in a given target tracking period k, the measuring mechanism of narrowband MIMO radars[2] can be modeled as [19, Eq. (11)], [60, p. 439], [49],

$$\begin{aligned}\mathbf{y}(t) \quad &= \beta_0 \boldsymbol{b}(\theta_0)\boldsymbol{a}^{\mathsf{H}}(\theta_0)\mathbf{s}(t-\tau_0)e^{j2\pi\nu_0 t} + \\ &\quad \sum_{i=1}^{N_s} \beta_{i,0}\boldsymbol{b}(\theta_{i,0})\boldsymbol{a}^{\mathsf{H}}(\theta_{i,0})\mathbf{s}(t-\tau_{i,0})e^{j2\pi\nu_{i,0}t} + \mathbf{n}(t),\end{aligned} \tag{2}$$

where t, $0 \le t \le T_i \le T_t$, denotes the radar's logical time of signal processing in a CPI; β_0 is the path gain of the ToI; N_s is the total number of scatterers (including, e.g., targets of no interest); $\beta_{i,0}$, $\theta_{i,0}$, $\tau_{i,0}$, and $\nu_{i,0}$ are the parameters of the i^{th} scatterer; $\mathbf{s}(t) \in \mathbb{C}^{N_t}$ denotes the transmitted waveform at time t, $\mathbf{y}(t) \in \mathbb{C}^{N_r}$ the received signal, and $\mathbf{n}(t) \in \mathbb{C}^{N_r}$

[2]When a wireless system is narrowband in terms of radar sensing, it may still be treated as broadband in terms of communications; for determination criteria, see [19, Eq. (3)], [60, p. 439].

the zero-mean circularly-symmetric complex Gaussian channel noise vector. For a target tracking problem aiming to resolve target parameters $(\tau_0, \nu_0, \theta_0)$, (2) can be compactly written as

$$\mathbf{y}(t) \quad = \beta_0 \boldsymbol{b}(\theta_0)\boldsymbol{a}^{\mathsf{H}}(\theta_0)\mathbf{s}(t-\tau_0)e^{j2\pi\nu_0 t} + \mathbf{n}_c(t), \tag{3}$$

where $\mathbf{n}_c(t) \in \mathbb{C}^{N_r}$ denotes the channel interference-plus-noise (IPN) vector, which is not necessarily Gaussian. Supposing that the Doppler frequency shift is piece-wise constant across different PRIs, (3) can be sampled at $t = pT_r + lT_s$, leading to the discrete-time representation

$$\mathbf{y}_p(l) \quad = \beta_0 \boldsymbol{b}(\theta_0)\boldsymbol{a}^{\mathsf{H}}(\theta_0)\mathbf{s}_p(l-\tau_0)e^{j2\pi\nu_0 pT_r} + \mathbf{n}_{c,p}(l), \tag{4}$$

where $p \in [N_p]$ is the slow-time Doppler-bin index and $l \in [L]$ is the fast-time range-bin index; $\mathbf{s}_p(l)$ is the sampled transmitted waveform at p^{th} PRI and l^{th} range bin, $\mathbf{y}_p(l)$ the sampled received signal, and $\mathbf{n}_{c,p}(l)$ the sampled channel IPN vector. To avoid notational clutter, $\mathbf{s}_p(l-\tau_0)$ is shorthand for $\mathbf{s}_p(l-\langle\tau_0/T_s\rangle)$. The phase variation term $e^{j2\pi\nu_0 lT_s}$ is ignored.

At times, the frequency-domain representation of (4) would be computationally useful. Suppose that we have N_{cr} FFT points for ranging. Let the frequency-bin width be $\Delta \coloneqq B/N_{\text{cr}}$. Then, the frequency-domain representation of (4) is

$$\begin{aligned}\bar{\mathbf{y}}_p(n) \quad &= \beta_0 \boldsymbol{b}(\theta_0)\boldsymbol{a}^{\mathsf{H}}(\theta_0)\bar{\mathbf{s}}_p(n)e^{-j2\pi n\Delta\tau_0}e^{j2\pi pT_r\nu_0} + \\ &\quad \bar{\mathbf{n}}_{c,p}(n),\end{aligned} \tag{5}$$

where $n \in [N_{\text{cr}}]$ denotes the frequency-bin index, $\bar{\mathbf{y}}_p$ the FFT of $\mathbf{y}_p$, $\bar{\mathbf{s}}_p$ the FFT of $\mathbf{s}_p$, and $\bar{\mathbf{n}}_{c,p}$ the FFT of $\mathbf{n}_{c,p}$; the n-independent phase term $e^{-j2\pi[f_c - \frac{(N_{\text{cr}}-1)}{2}\Delta]\tau_0}$ has been absorbed by β_0. In matched filtering for ranging, it is common that $N_{\text{cr}} = L$. However, the computational complexity in the time domain is $\mathcal{O}(L^2)$, while that in the frequency domain is $\mathcal{O}(L\log_2(L))$ due to the FFT technique.

In signal-level target tracking (SLTR), (4) or (5) defines the state measurement equation in the tracking model (1). To be specific, $\mathbf{y}_k$ is a data set constructed as

$$\mathbf{y}_k \coloneqq \begin{cases} \{\mathbf{y}_p(l)\}_{\forall p,l}, & \text{if time-domain processing,} \\ \{\bar{\mathbf{y}}_p(n)\}_{\forall p,n}, & \text{if frequency-domain processing,} \end{cases} \tag{6}$$

where the notational dependence of the right-hand-side terms on the tracking period index k is omitted.

Under the Bayesian statistical inference paradigm, the target tracking problem using the system model (1), in a specific time k, can be stated as finding the posterior distribution

$$q(\boldsymbol{x}_k|\mathcal{Y}_k) \propto q(\boldsymbol{y}_k|\boldsymbol{x}_k)q(\boldsymbol{x}_k|\mathcal{Y}_{k-1}) \tag{7}$$

of the unknown state vector $\mathbf{x}_k$ by utilizing the likelihood function $\boldsymbol{x}_k \mapsto q(\boldsymbol{y}_k|\boldsymbol{x}_k)$ and the prior distribution $q(\boldsymbol{x}_k|\mathcal{Y}_{k-1})$; at every k, the unknown true state vector $\boldsymbol{x}_{0,k}$ is one-to-one corresponded to the true target parameters $(\tau_{0,k}, \nu_{0,k}, \theta_{0,k})$. It is preferable if $q(\boldsymbol{x}_k|\mathcal{Y}_k)$ can concentrate around the true state $\boldsymbol{x}_{0,k}$. The prior distribution $q(\boldsymbol{x}_k|\mathcal{Y}_{k-1})$ is induced by the state transition equation, while the likelihood function $q(\boldsymbol{y}_k|\boldsymbol{x}_k)$ is defined by the state measurement equation. In this section, for notational simplicity, we suppress the dependence on the time index k and the measurement history $\mathcal{Y}_{k-1}$. Eq. (7) is therefore shorthanded as

$$q(\boldsymbol{x}|\boldsymbol{y}) \propto q(\boldsymbol{y}|\boldsymbol{x})q(\boldsymbol{x}). \tag{8}$$

Focusing on the target parameters, (8) particularizes into

$$q(\boldsymbol{\varphi}|\boldsymbol{y}) \propto q(\boldsymbol{y}|\boldsymbol{\varphi})q(\boldsymbol{\varphi}), \tag{9}$$

where $\boldsymbol{\varphi} \coloneqq (\tau, \nu, \theta) \in \mathbb{R}^3$ and the likelihood function $\boldsymbol{\varphi} \mapsto q(\boldsymbol{y}|\boldsymbol{\varphi})$ is induced by either (4) or (5); cf. (6).

B. Problem Statements (Research Gaps in SLTR)

In applying the Bayes' rule (9) to signal-level target tracking, the real-world operational dilemma is twofold:

- The explicit and exact mathematical expression of the likelihood function $\boldsymbol{\varphi} \mapsto q(\boldsymbol{y}|\boldsymbol{\varphi})$ is difficult to obtain because the probabilistic models of β_0, $\mathbf{n}_{c,p}(l)$, and $\bar{\mathbf{n}}_{c,p}(n)$ are challenging to specify in practice. Even if the probabilistic form of $q(\boldsymbol{y}|\boldsymbol{\varphi})$ is (assumed to be) known, for example, Gaussian or exponential family, its statistical information, such as mean and covariance, is still to be meticulously calibrated by leveraging the domain knowledge and historical data. The complication arises if $q(\boldsymbol{y}|\boldsymbol{\varphi})$ is time-varying across different tracking periods due to the significant maneuvers of the ToI and scatterers and to the change of channel conditions.
- To simplify the modeling of $q(\boldsymbol{y}|\boldsymbol{\varphi})$, some statistical inference methods, such as conventional particle filters, treat β_0 as a nuisance parameter to be jointly estimated from the collected data [40], [41]. This scheme leads to the augmented parameter vector $\boldsymbol{\varphi} \coloneqq (\text{real}(\beta), \text{imag}(\beta), \tau, \nu, \theta) \in \mathbb{R}^5$ of the ToI. However, although convenient for modeling, this augmentation significantly introduces additional computational burdens to statistical inference because the larger the dimension of the state vector $\mathbf{x}_k$ is, the lower the computational and sample efficiency of any statistical inference method would be. This is specifically the case for particle filters where more particles, and therefore more computational resources, must be employed to guarantee a satisfactory accuracy for $(\tau_0, \nu_0, \theta_0) \in \mathbb{R}^3$ [50], [51]. Although the Rao-Blackwellized particle filtering can be used to reduce such computational burdens [52], it is inadequate if β_0 abruptly varies across consecutive tracking periods k: Note that to track an unknown parameter, it should remain almost constant or slowly vary over time k [37, p. 397].

To address the above two issues, this article revolutionizes the existing particle filtering framework for signal-level target tracking using MIMO pulse-Doppler radar and proposes a new PF-SLTR scheme.

III. A New Particle Filter for Signal-Level Target Tracking

A. Optimization-Centric Interpretation of Bayes' Rule (9)

In the statistical machine learning and general statistics communities, a well-established optimization-centric interpre-

tation of the Bayes' rule (9) is as follows:

$$q(\boldsymbol{\varphi}|\boldsymbol{y}) = \underset{u(\boldsymbol{\varphi})}{\operatorname{argmin}} \mathbb{E}_{\boldsymbol{\varphi}\sim u(\boldsymbol{\varphi})}[-\ln q(\boldsymbol{y}|\boldsymbol{\varphi})] + \mathrm{KL}[u(\boldsymbol{\varphi})\|q(\boldsymbol{\varphi})], \tag{10}$$

where $u(\boldsymbol{\varphi})$ is a variable distribution of $\boldsymbol{\varphi}$ and $\mathrm{KL}[u(\boldsymbol{\varphi})\|q(\boldsymbol{\varphi})]$ defines the Kullback–Leibler divergence of $u(\boldsymbol{\varphi})$ from $q(\boldsymbol{\varphi})$. Eq. (10) indicates that the posterior distribution $q(\boldsymbol{\varphi}|\boldsymbol{y})$ of $\boldsymbol{\varphi}$, given $\boldsymbol{y}$, *maximizes* the expected log-likelihood evaluated at $\boldsymbol{y}$, and simultaneously, *minimizes* the dissimilarity from the prior distribution $q(\boldsymbol{\varphi})$. This interpretation aligns well with our intuition: the posterior distribution should mostly match the "data evidence" at hand (i.e., maximum likelihood), and at the same time, mostly match the "prior knowledge" in the brain (i.e., minimum deviation from the prior).

Eq. (10) can be generalized to the following formulation

$$q(\boldsymbol{\varphi}|\boldsymbol{y}) \coloneqq \underset{u(\boldsymbol{\varphi})}{\operatorname{argmin}} \mathbb{E}_{\boldsymbol{\varphi}\sim u(\boldsymbol{\varphi})}\xi\rho(\boldsymbol{y},\boldsymbol{\varphi}) + \mathrm{KL}[u(\boldsymbol{\varphi})\|q(\boldsymbol{\varphi})], \tag{11}$$

where $\rho(\boldsymbol{y},\boldsymbol{\varphi})$ is a general cost function that encodes the $\boldsymbol{y}$-data evidence of $\boldsymbol{\varphi}$, beyond the well-adopted negative log-likelihood cost function $-\ln q(\boldsymbol{y}|\boldsymbol{\varphi})$, and $\xi \geq 0$ is a tradeoff parameter that balances between $\boldsymbol{y}$-data evidence and $q(\boldsymbol{\varphi})$-prior information. In (11), with a slight abuse of notation, we reuse $q(\boldsymbol{\varphi} \mid \boldsymbol{y})$ to denote a generalized posterior distribution; cf. (10), where $q(\boldsymbol{\varphi} \mid \boldsymbol{y})$ refers to the conventional Bayesian posterior. The generalization from (10) to (11) is rooted in the following two motivations:

- Different applications prefer different utility metrics, so we can manipulate how the available data $\boldsymbol{y}$ supports the utility of the solution (or decision) $\boldsymbol{\varphi}$. The basic principle to design ρ is that, if $\boldsymbol{\varphi}_1$ is favored over $\boldsymbol{\varphi}_2$ given $\boldsymbol{y}$, we should have $\rho(\boldsymbol{y},\boldsymbol{\varphi}_1) \leq \rho(\boldsymbol{y},\boldsymbol{\varphi}_2)$. Illustrating instances in machine learning applications can be seen in [54].
- In practice, the likelihood function $q(\boldsymbol{y}|\boldsymbol{\varphi})$ may not be exactly specified, so we can steer the cost function ρ to achieve robustness against this likelihood-model mismatch. Examples in this direction can be seen in [56].

A desired property of (11) is that it admits a closed-form solution for every cost function $\rho(\boldsymbol{y},\boldsymbol{\varphi})$ and every prior distribution $q(\boldsymbol{\varphi})$, which is beneficial in real-time signal processing, such as online target tracking.

Lemma 1 (see [55]): The generalized posterior distribution $q(\boldsymbol{\varphi}|\boldsymbol{y})$ solving (11) is given by

$$q(\boldsymbol{\varphi}|\boldsymbol{y}) \propto q(\boldsymbol{\varphi})e^{-\xi\rho(\boldsymbol{y},\boldsymbol{\varphi})}, \tag{12}$$

if the normalizer of the right-hand-side term exists. □

Eq. (12) is called the *Gibbs posterior* in the literature. Focusing back on the Bayesian filtering for signal-level target tracking (e.g., PF-SLTR), since the exact likelihood function $\boldsymbol{\varphi} \mapsto q(\boldsymbol{y}|\boldsymbol{\varphi})$ is unavailable, we are motivated to construct an appropriate cost function $\rho(\boldsymbol{y},\boldsymbol{\varphi})$ to solve the two issues stated before, that is, without relying on the exact knowledge of the likelihood function $\boldsymbol{\varphi} \mapsto q(\boldsymbol{y}|\boldsymbol{\varphi})$ and without augmenting nuisance parameters $(\mathrm{real}(\beta), \mathrm{imag}(\beta))$ into $\boldsymbol{\varphi}$.

B. A New Framework of PF-SLTR

Particle filtering, which utilizes particle representations of probability density functions, is a computational method of Bayesian filtering [38], [39]. To be specific, in particle filtering, the prior distribution $q(\boldsymbol{\varphi})$ is represented by a set of discrete particles $\{\boldsymbol{\varphi}_0, \boldsymbol{\varphi}_1, \ldots, \boldsymbol{\varphi}_{N_{\text{par}}-1}\}$:

$$q(\boldsymbol{\varphi}) = \sum_{i=0}^{N_{\text{par}}-1} \eta_i \delta(\boldsymbol{\varphi} - \boldsymbol{\varphi}_i), \tag{13}$$

where $\eta_i \in [0,1]$ is the prior weight associated with the particle $\boldsymbol{\varphi}_i$, $\sum_{i=0}^{N_{\text{par}}-1} \eta_i = 1$, and $\delta(\cdot)$ is the Dirac delta distribution. Then, under the Gibbs rule (12), the posterior distribution $q(\boldsymbol{\varphi}|\boldsymbol{y})$ given $\boldsymbol{y}$ can be represented as

$$q(\boldsymbol{\varphi}|\boldsymbol{y}) = \sum_{i=0}^{N_{\text{par}}-1} u_i \delta(\boldsymbol{\varphi} - \boldsymbol{\varphi}_i), \tag{14}$$

where $u_i \in [0,1]$ is the posterior weight associated with the particle $\boldsymbol{\varphi}_i$, $\sum_{i=0}^{N_{\text{par}}-1} u_i = 1$, and for every $i \in [N_{\text{par}}]$, we have

$$u_i \propto \eta_i e^{-\xi\rho(\boldsymbol{y},\boldsymbol{\varphi}_i)}. \tag{15}$$

Example 1: If the likelihood function can be exactly specified, i.e., $\rho(\boldsymbol{y},\boldsymbol{\varphi}) \coloneqq -\ln q(\boldsymbol{y}|\boldsymbol{\varphi})$, by setting $\xi \coloneqq 1$, (15) particularizes to

$$u_i \propto \eta_i \cdot q(\boldsymbol{y}|\boldsymbol{\varphi}_i) = \eta_i \cdot e^{-[-\ln q(\boldsymbol{y}|\boldsymbol{\varphi}_i)]}, \tag{16}$$

which is the usual particle filter. □

Eqs. (13)-(15) form the foundation of our new particle filtering framework for signal-level target tracking. The enabling yet challenging step is to design a cost function $\rho(\boldsymbol{y},\boldsymbol{\varphi})$ without relying on the true likelihood function $q(\boldsymbol{y}|\boldsymbol{\varphi})$. In addition, this cost function satisfies the following rule.

Rule 1: At data $\boldsymbol{y}$, it holds that

$$\rho(\boldsymbol{y},\boldsymbol{\varphi}_1) \leq \rho(\boldsymbol{y},\boldsymbol{\varphi}_2), \tag{17}$$

or equivalently,

$$e^{-\rho(\boldsymbol{y},\boldsymbol{\varphi}_1)} \geq e^{-\rho(\boldsymbol{y},\boldsymbol{\varphi}_2)}, \tag{18}$$

if $\boldsymbol{\varphi}_1$ is preferred over $\boldsymbol{\varphi}_2$. □

Aligning with Rule 1, in what follows, this article suggests four concrete cost functions for PF-SLTR, which are conceptually and operationally simple for MIMO pulse-Doppler radars described by (2)−(6).

1) Cost Functions in PF-SLTR: The first two cost functions are motivated by the least-squares estimation.

Method 1: If we work with the time-domain signals in (4), we define

$$\rho_1(\boldsymbol{y},\boldsymbol{\varphi}) \coloneqq \min_{\gamma\in\mathbb{C}} \sum_{p=0}^{N_p-1} \sum_{l=0}^{L-1} \left\| \boldsymbol{y}_p(l) - \gamma \boldsymbol{b}(\theta)\boldsymbol{a}^{\mathsf{H}}(\theta)\boldsymbol{s}_p(l-\tau)e^{j2\pi p T_r \nu} \right\|_2^2, \tag{19}$$

where $\boldsymbol{y}$ is a realized sample of the radar received signal $\mathbf{y}_k$ in (6), $\boldsymbol{\varphi} \coloneqq (\tau,\nu,\theta) \in \mathbb{R}^3$ is a hypothesized ToI-parameter vector, and $\boldsymbol{y}_p(l)$ is a realized sample of $\mathbf{y}_p(l)$ in (4). □

In $\rho_1(\boldsymbol{y},\boldsymbol{\varphi})$, the nuisance parameter γ is marginalized out through the least-squares principle (i.e., the minimization operation). Different from Rao-Blackwellization, this operation can serve as an alternative approach to dimensionality

reduction in particle filtering. The cost function $\rho_1(\boldsymbol{y},\boldsymbol{\varphi})$ can be computationally simplified.

Proposition 1: If the transmit array has the empirical spatial correlation $\hat{\boldsymbol{R}}_s$, then $\rho_1(\boldsymbol{y},\boldsymbol{\varphi})$ equals

$$\rho_1(\boldsymbol{y},\boldsymbol{\varphi}) = \sum_{p=0}^{N_p-1}\sum_{l=0}^{L-1}\boldsymbol{y}_p^{\mathsf{H}}(l)\boldsymbol{y}_p(l) \quad - \frac{\left|\sum_{p=0}^{N_p-1}\sum_{l=0}^{L-1}\boldsymbol{y}_p^{\mathsf{H}}(l)\boldsymbol{b}(\theta)\boldsymbol{a}^{\mathsf{H}}(\theta)\boldsymbol{s}_p(l-\tau)e^{j2\pi pT_r\nu}\right|^2}{N_rN_pL_{\text{ss}}\boldsymbol{a}^{\mathsf{H}}(\theta)\hat{\boldsymbol{R}}_s\boldsymbol{a}(\theta)}, \tag{20}$$

where L_{ss} denotes the number of snapshots contained in the pulse $\{\boldsymbol{s}_p(l)\}_{\forall l\in[L_{\text{ss}}]}$, for every $p\in[N_p]$. When $\hat{\boldsymbol{R}}_s = P_t\boldsymbol{I}_{N_t}$, the denominator becomes $P_tN_tN_rN_pL_{\text{ss}}$, which is $\boldsymbol{\varphi}$-independent.

Proof: See Appendix A in the online supplementary materials. □

Method 2: If we work with the frequency-domain signals in (5), we define

$$\rho_2(\boldsymbol{y},\boldsymbol{\varphi}) \coloneqq \min_{\gamma\in\mathbb{C}}\sum_{p=0}^{N_p-1}\sum_{n=0}^{N_{\text{cr}}-1}\left\|\bar{\boldsymbol{y}}_p(n) - \gamma\boldsymbol{b}(\theta)\boldsymbol{a}^{\mathsf{H}}(\theta)\bar{\boldsymbol{s}}_p(n)e^{-j2\pi n\Delta\tau}e^{j2\pi pT_r\nu}\right\|_2^2, \tag{21}$$

where $\boldsymbol{y}$ is a realized sample of the radar received signal $\mathbf{y}_k$ in (6), $\boldsymbol{\varphi}\coloneqq(\tau,\nu,\theta)\in\mathbb{R}^3$ is a hypothesized ToI-parameter vector, and $\bar{\boldsymbol{y}}_p(n)$ is a realized sample of $\bar{\mathbf{y}}_p(n)$ in (5). □

Due to the minimization operation over γ, by employing $\rho_2(\boldsymbol{y},\boldsymbol{\varphi})$, dimensionality reduction in particle filtering is implicitly conducted; cf. Rao-Blackwellization. The cost function $\rho_2(\boldsymbol{y},\boldsymbol{\varphi})$ can be computationally simplified as follows.

Proposition 2: If the transmit array has the empirical spatial correlation $\hat{\boldsymbol{R}}_s$, then $\rho_2(\boldsymbol{y},\boldsymbol{\varphi})$ equals

$$\rho_2(\boldsymbol{y},\boldsymbol{\varphi}) = \sum_{p=0}^{N_p-1}\sum_{n=0}^{N_{\text{cr}}-1}\bar{\boldsymbol{y}}_p^{\mathsf{H}}(n)\bar{\boldsymbol{y}}_p(n) \quad - \frac{\left|\sum_{p=0}^{N_p-1}\sum_{n=0}^{N_{\text{cr}}-1}\bar{\boldsymbol{y}}_p^{\mathsf{H}}(n)\boldsymbol{b}(\theta)\boldsymbol{a}^{\mathsf{H}}(\theta)\bar{\boldsymbol{s}}_p(n)e^{-j2\pi n\Delta\tau}e^{j2\pi pT_r\nu}\right|^2}{N_rN_pN_{\text{cr}}\boldsymbol{a}^{\mathsf{H}}(\theta)\hat{\boldsymbol{R}}_s\boldsymbol{a}(\theta)}, \tag{22}$$

where N_{cr} denotes the number of frequency bins (i.e., FFT points) to represent $\{\bar{\boldsymbol{s}}_p(n)\}_{\forall n\in[N_{\text{cr}}]}$, for every $p\in[N_p]$. When $\hat{\boldsymbol{R}}_s = P_t\boldsymbol{I}_{N_t}$, the denominator in the second line becomes $P_tN_tN_rN_pN_{\text{cr}}$, which is $\boldsymbol{\varphi}$-independent.

Proof: Similar to the proof of Proposition 1. □

As we can see from Propositions 1 and 2, to expect small values of $\rho_1(\boldsymbol{y},\boldsymbol{\varphi})$ and $\rho_2(\boldsymbol{y},\boldsymbol{\varphi})$ when given $\boldsymbol{y}$, it suffices to have large values of

$$\frac{\left|\sum_{p=0}^{N_p-1}\sum_{l=0}^{L-1}\boldsymbol{y}_p^{\mathsf{H}}(l)\boldsymbol{b}(\theta)\boldsymbol{a}^{\mathsf{H}}(\theta)\boldsymbol{s}_p(l-\tau)e^{j2\pi pT_r\nu}\right|^2}{N_rN_pL_{\text{ss}}\boldsymbol{a}^{\mathsf{H}}(\theta)\hat{\boldsymbol{R}}_s\boldsymbol{a}(\theta)} \tag{23}$$

and

$$\frac{\left|\sum_{p=0}^{N_p-1}\sum_{n=0}^{N_{\text{cr}}-1}\bar{\boldsymbol{y}}_p^{\mathsf{H}}(n)\boldsymbol{b}(\theta)\boldsymbol{a}^{\mathsf{H}}(\theta)\bar{\boldsymbol{s}}_p(n)e^{-j2\pi n\Delta\tau}e^{j2\pi pT_r\nu}\right|^2}{N_rN_pN_{\text{cr}}\boldsymbol{a}^{\mathsf{H}}(\theta)\hat{\boldsymbol{R}}_s\boldsymbol{a}(\theta)}, \tag{24}$$

in (20) and (22), respectively, because $\rho_1(\boldsymbol{y},\boldsymbol{\varphi})\geq 0$ and $\rho_2(\boldsymbol{y},\boldsymbol{\varphi})\geq 0$ naturally hold for all $(\boldsymbol{y},\boldsymbol{\varphi})$. The two numerators are exactly the ambiguity functions (i.e., the matched filters) for MIMO pulse-Doppler radars in the time domain and frequency domain, respectively [19, Eq. (33)], [61, p. 131]. However, the two denominators introduce modifiers that depend on the spatial correlation matrix $\hat{\boldsymbol{R}}_s$ and the DoA θ.

In what follows, for brevity in presentation and without loss of generality, we assume that $\hat{\boldsymbol{R}}_s \coloneqq P_t\boldsymbol{I}_{N_t}$. That is, the transmit waveforms are uncorrelated across antennas. In this case, it suffices to have large values for the numerators in (23) and (24), respectively, because the two denominators degenerate to constants. This observation inspires the next two cost functions.

Method 3: If we work with the time-domain signals in (4), we define

$$\rho_3(\boldsymbol{y},\boldsymbol{\varphi}) \coloneqq -\ln\left[\left|\sum_{p=0}^{N_p-1}\sum_{l=0}^{L-1}\boldsymbol{y}_p^{\mathsf{H}}(l)\boldsymbol{b}(\theta)\boldsymbol{a}^{\mathsf{H}}(\theta)\boldsymbol{s}_p(l-\tau)e^{j2\pi pT_r\nu}\right|^2\right], \tag{25}$$

where $\boldsymbol{y}$ is a realized sample of the radar received signal $\mathbf{y}_k$ in (6), $\boldsymbol{\varphi}\coloneqq(\tau,\nu,\theta)\in\mathbb{R}^3$ is a hypothesized ToI-parameter vector, and $\boldsymbol{y}_p(l)$ is a realized sample of $\mathbf{y}_p(l)$ in (4). □

Using Method 3, (15) becomes

$$u_i \propto \eta_i\cdot\left|\sum_{p=0}^{N_p-1}\sum_{l=0}^{L-1}\boldsymbol{y}_p^{\mathsf{H}}(l)\boldsymbol{b}(\theta_i)\boldsymbol{a}^{\mathsf{H}}(\theta_i)\boldsymbol{s}_p(l-\tau_i)e^{j2\pi pT_r\nu_i}\right|^{2\xi}, \tag{26}$$

where (τ_i,ν_i,θ_i) denotes the i^{th} particle. Eq. (26) aligns well with our intuition because, the closer the parameter pair (τ_i,ν_i,θ_i) is to its true value (τ_0,ν_0,θ_0), the larger the value of the ambiguity function evaluated at (τ_i,ν_i,θ_i), and thus the more the collected radar data $\boldsymbol{y}$ supports the i^{th} particle. If $\hat{\boldsymbol{R}}_s\neq P_t\boldsymbol{I}_{N_t}$, the denominator $N_rN_pL_{\text{ss}}\boldsymbol{a}^{\mathsf{H}}(\theta)\hat{\boldsymbol{R}}_s\boldsymbol{a}(\theta)$ should be retained in the right-hand side of (26).

Method 4: If we work with the frequency-domain signals in (5), we define

$$\rho_4(\boldsymbol{y},\boldsymbol{\varphi}) \coloneqq -\ln\left[\left|\sum_{p=0}^{N_p-1}\sum_{n=0}^{N_{\text{cr}}-1}\bar{\boldsymbol{y}}_p^{\mathsf{H}}(n)\boldsymbol{b}(\theta)\boldsymbol{a}^{\mathsf{H}}(\theta)\bar{\boldsymbol{s}}_p(n)e^{-j2\pi n\Delta\tau}e^{j2\pi pT_r\nu}\right|^2\right], \tag{27}$$

where $\boldsymbol{y}$ is a realized sample of the radar received signal $\mathbf{y}_k$ in (6), $\boldsymbol{\varphi}\coloneqq(\tau,\nu,\theta)\in\mathbb{R}^3$ is a hypothesized ToI-parameter vector, and $\bar{\boldsymbol{y}}_p(n)$ is a realized sample of $\bar{\mathbf{y}}_p(n)$ in (5). □

Using Method 4, (15) becomes

$$u_i \quad \propto \eta_i \cdot \left| \sum_{p=0}^{N_p-1} \sum_{n=0}^{N_{\text{cr}}-1} \bar{\boldsymbol{y}}_p^{\mathsf{H}}(n)\boldsymbol{b}(\theta_i)\boldsymbol{a}^{\mathsf{H}}(\theta_i)\bar{\boldsymbol{s}}_p(n)e^{-j2\pi n\Delta\tau_i}e^{j2\pi pT_r\nu_i}\right|^{2\xi}. \tag{28}$$

Similarly, the closer the parameter pair $(\tau_i, \nu_i, \theta_i)$ is to its true value $(\tau_0, \nu_0, \theta_0)$, the larger the value of the ambiguity function evaluated at $(\tau_i, \nu_i, \theta_i)$, and thus the more the collected radar data $\boldsymbol{y}$ supports the i^{th} particle. If $\hat{\boldsymbol{R}}_s \neq P_t\boldsymbol{I}_{N_t}$, the denominator $N_rN_pN_{\text{cr}}\boldsymbol{a}^{\mathsf{H}}(\theta)\hat{\boldsymbol{R}}_s\boldsymbol{a}(\theta)$ should be retained in the right-hand side of (28).

The cost functions $\rho_3(\boldsymbol{y}, \boldsymbol{\varphi})$ and $\rho_4(\boldsymbol{y}, \boldsymbol{\varphi})$ are conceptually consistent with $\rho_1(\boldsymbol{y}, \boldsymbol{\varphi})$ and $\rho_2(\boldsymbol{y}, \boldsymbol{\varphi})$ when $\hat{\boldsymbol{R}}_s = P_t\boldsymbol{I}_{N_t}$; cf. Propositions 1 and 2. However, $\rho_3(\boldsymbol{y}, \boldsymbol{\varphi})$ and $\rho_4(\boldsymbol{y}, \boldsymbol{\varphi})$ are computationally more lightweight than $\rho_1(\boldsymbol{y}, \boldsymbol{\varphi})$ and $\rho_2(\boldsymbol{y}, \boldsymbol{\varphi})$, especially when implementing the Gibbs-posterior-based PF-SLTR; see (26) and (28). To limit the computational complexity, hereafter, this article focuses on the cost functions $\rho_3(\boldsymbol{y}, \boldsymbol{\varphi})$ and $\rho_4(\boldsymbol{y}, \boldsymbol{\varphi})$. In this sense, hence, the cost functions $\rho_1(\boldsymbol{y}, \boldsymbol{\varphi})$ and $\rho_2(\boldsymbol{y}, \boldsymbol{\varphi})$ in this article are more analytically motivational than practically instructive: They motivate the proposals of $\rho_3(\boldsymbol{y}, \boldsymbol{\varphi})$ and $\rho_4(\boldsymbol{y}, \boldsymbol{\varphi})$, respectively.

2) Property Analysis: In this subsection, we analyze the properties of the proposed cost functions. As elucidated before, we are particularly interested in $\rho_3(\boldsymbol{y}, \boldsymbol{\varphi})$ and $\rho_4(\boldsymbol{y}, \boldsymbol{\varphi})$ for their computational advantages. Since $\rho_3(\boldsymbol{y}, \boldsymbol{\varphi})$ and $\rho_4(\boldsymbol{y}, \boldsymbol{\varphi})$ are mathematically equivalent under FFT and inverse FFT (IFFT), it suffices to analyze the property of $\rho_4(\boldsymbol{y}, \boldsymbol{\varphi})$ only. The proposition below shows that $\rho_4(\boldsymbol{y}, \boldsymbol{\varphi})$ aligns with Rule 1 in a well-specified tracking gate. A tracking gate (or validation gate) is a hypothesized region in which the ToI is assumed to be located; that is, it is a delimited subspace of $\mathbb{R}^3$ in which the true target parameters $(\tau_0, \nu_0, \theta_0)$ are included.

Proposition 3: Suppose that the transmitted signals are spatially uncorrelated with $\boldsymbol{R}_s \coloneqq \mathbb{E}\bar{\mathbf{s}}_p(n)\bar{\mathbf{s}}_p^{\mathsf{H}}(n) = P_t\boldsymbol{I}_{N_t}$, for every $p \in [N_p]$ and $n \in [N_{\text{cr}}]$, and scatterers are well-separated from the ToI.[3] Additionally, we suppose that the transmitter and the receiver are uniform linear arrays with half-wavelength spacing: that is,

$$\boldsymbol{a}(\theta) \coloneqq [1, e^{-j\pi\sin\theta}, \ldots, e^{-j\pi(N_t-1)\sin\theta}]^{\mathsf{T}}, \tag{29}$$

and

$$\boldsymbol{b}(\theta) \coloneqq [1, e^{-j\pi\sin\theta}, \ldots, e^{-j\pi(N_r-1)\sin\theta}]^{\mathsf{T}}. \tag{30}$$

Let $N_{tr} \coloneqq \max\{N_t, N_r\}$. Then, within the tracking gate

$$\left[\tau_0 - \frac{1}{B},\ \tau_0 + \frac{1}{B}\right] \times \left[\nu_0 - \frac{1}{T_i},\ \nu_0 + \frac{1}{T_i}\right] \times \left[\arcsin\left(\sin\theta_0 - \frac{2}{N_{tr}}\right),\ \arcsin\left(\sin\theta_0 + \frac{2}{N_{tr}}\right)\right], \tag{31}$$

[3]Well-separation means that the energy from scatterers that leaks into the ToI's tracking gate through the matched filter's sidelobes is negligible.

the cost function

$$-\ln\left[\left|\sum_{p=0}^{N_p-1}\sum_{n=0}^{N_{\text{cr}}-1}\mathbb{E}_{\bar{\mathbf{y}}_p(n),\bar{\mathbf{s}}_p(n)}\left[\bar{\mathbf{y}}_p^{\mathsf{H}}(n)\boldsymbol{b}(\theta)\boldsymbol{a}^{\mathsf{H}}(\theta)\bar{\mathbf{s}}_p(n)e^{-j2\pi n\Delta\tau}e^{j2\pi pT_r\nu}\right]\right|^2\right], \tag{32}$$

induced by $\rho_4(\boldsymbol{y}, \boldsymbol{\varphi})$ in (27), through inner-expectation over $\bar{\mathbf{y}}_p(n)$ and $\bar{\mathbf{s}}_p(n)$, satisfies Rule 1.

Proof: See Appendix B in the online supplementary materials. □

Due to the randomness of $\bar{\mathbf{y}}_p(n)$ and $\bar{\mathbf{s}}_p(n)$, we resort to the expected version in (32) for property analysis, to be specific, the analysis on the statistical property instead of the single-sample property. In the practice of PF-SLTR, however, (27) should be used to update the weights of the particles; see (28).

In addition, the assumptions in Proposition 3 are introduced primarily to obtain a clean statistical characterization of the proposed cost function. The separated-scatterer assumption means that the leakage from other scatterers into the ToI's tracking gate is negligible, so that the ambiguity-function response around the ToI is dominated by the ToI component. If this condition is not satisfied, nearby scatterers may distort the cost-function landscape and mislead the tracking filter. Similarly, the uncorrelated-waveform assumption $\boldsymbol{R}_s \coloneqq P_t\boldsymbol{I}_{N_t}$ is used to simplify the cost functions. To be specific, if $\boldsymbol{R}_s \neq P_t\boldsymbol{I}_{N_t}$, the corresponding denominators involving $\boldsymbol{a}^{\mathsf{H}}(\theta)\hat{\boldsymbol{R}}_s\boldsymbol{a}(\theta)$ should be retained, as in (23) and (24). In summary, when $\boldsymbol{R}_s$, $\boldsymbol{a}$, and $\boldsymbol{b}$ take more complicated forms, the tracking gate and cost functions should be calculated accordingly. For clarity of statistical analysis, Proposition 3 is established under these controlled assumptions to provide an interpretable analytical result.

Next, we investigate the role of the parameter ξ in (26) and (28). Let $\boldsymbol{\alpha} \coloneqq [\alpha_0, \alpha_1, \ldots, \alpha_{N_{\text{par}}-1}] > 0$ denote the N_{par}-dimensional data-evidence vector of particles, which is normalized so that its sum equals one; hence, $\boldsymbol{\alpha}$ can be regarded as a discrete probability vector. Taking (26) as an example, up to a normalizing constant, we can define

$$\alpha_i \propto \left|\sum_{p=0}^{N_p-1}\sum_{l=0}^{L-1}\boldsymbol{y}_p^{\mathsf{H}}(l)\boldsymbol{b}(\theta_i)\boldsymbol{a}^{\mathsf{H}}(\theta_i)\boldsymbol{s}_p(l-\tau_i)e^{j2\pi pT_r\nu_i}\right|^2,$$

resulting in the following rule for generating posterior weights:

$$u_i \propto \eta_i\alpha_i^{\xi}, \quad \forall i \in [N_{\text{par}}]. \tag{33}$$

Let $\boldsymbol{\alpha}^{(\xi)} \coloneqq [\alpha_0^{\xi}, \alpha_1^{\xi}, \ldots, \alpha_{N_{\text{par}}-1}^{\xi}]/C_{\xi}$ denote a new distribution powered by $\xi \geq 0$ from $\boldsymbol{\alpha}$, where $C_{\xi} \coloneqq \sum_{i=0}^{N_{\text{par}}-1}\alpha_i^{\xi}$ is the normalization factor. We have the following result regarding the entropy values of $\boldsymbol{\alpha}$ and $\boldsymbol{\alpha}^{(\xi)}$. Note that the larger (resp. smaller) the entropy value of a discrete distribution, the more uniform (resp. polarized) this distribution is.

Theorem 1: It holds that

$$-\sum_{i=0}^{N_{\text{par}}-1}\alpha_i\ln\alpha_i\begin{cases}\leq-\sum_{i=0}^{N_{\text{par}}-1}\alpha_i^{(\xi)}\ln\alpha_i^{(\xi)}, & \text{if } 0\leq\xi\leq 1;\\ \geq-\sum_{i=0}^{N_{\text{par}}-1}\alpha_i^{(\xi)}\ln\alpha_i^{(\xi)}, & \text{if } \xi\geq 1.\end{cases}$$

Proof: See Appendix C in the online supplementary materials, where the entropy function $\xi\mapsto-\sum_{i=0}^{N_{\text{par}}-1}\alpha_i^{(\xi)}\ln\alpha_i^{(\xi)}$ is shown to be monotonically decreasing in $\xi\geq 0$. □

Theorem 1 implies that when $0\leq\xi<1$, we make the $\boldsymbol{y}$-data evidence (i.e., the powered evidence values $\boldsymbol{\alpha}^{(\xi)}$) more balanced across all particles $\{\boldsymbol{x}_i\}_{\forall i\in[N_{\text{par}}]}$. In contrast, when $\xi>1$, we let the $\boldsymbol{y}$-data evidence be more concentrated on particles that have large evidence values. An illustrative example is given below.

Example 2: Let $\boldsymbol{\alpha}\coloneqq[0.2,0.5,0.3]$. If $\xi=0.5$, we have $\boldsymbol{\alpha}^{(0.5)}=[0.2628,0.4154,0.3218]$; if $\xi=2$, we have $\boldsymbol{\alpha}^{(2)}=[0.1053,0.6579,0.2368]$. As indicated, $\boldsymbol{\alpha}^{(0.5)}$ is more balanced (i.e., having smaller differences) than $\boldsymbol{\alpha}$, while $\boldsymbol{\alpha}^{(2)}$ is more polarized (i.e., having larger differences) than $\boldsymbol{\alpha}$. □

Since the conventional Bayes' rule is $u_i\propto\eta_i\alpha_i$, for all $i\in[N_{\text{par}}]$, where $\{\alpha_i\}$ denotes the likelihood and $\{\eta_i\}$ the prior, the posterior $\{u_i\}$ is shaped by the relative dispersion of these two terms. To be specific, if the likelihood $\{\alpha_i\}$ is more balanced (i.e., more uniform) than the prior $\{\eta_i\}$, the posterior remains closer to the prior. In the limiting case where all $\{\alpha_i\}$ are equal, the likelihood carries no information and does not impact the posterior. In contrast, if the likelihood $\{\alpha_i\}$ is more concentrated (i.e., more polarized) than the prior, the posterior is pulled toward the likelihood. In the limiting case where one of $\{\alpha_i\}$ equals one and all others are zeros, the posterior is entirely determined by the likelihood. Therefore, in the modified Bayes' rule (33), i.e., $u_i\propto\eta_i\alpha_i^{\xi}$, ξ plays a key role in balancing the influence of the prior and the data evidence, as it directly controls the dispersion of the data-evidence vector. This dispersion-based interpretation provides an alternative perspective on the role of ξ in trading off between $\{\eta_i\}$ and $\{\alpha_i\}$, distinct from but complementary to the optimization-based interpretation in (11).

On the other hand, balanced prior and data-evidence vectors lead to balanced posterior weights, which in turn can benefit combating particle degeneracy, provided that particles are diverse and informative. In particle filtering, to ensure diversity and informativity, particles should be drawn from a well-designed proposal distribution [38, pp. 178-180].

IV. PF-SLTR for MIMO-OFDM ISAC

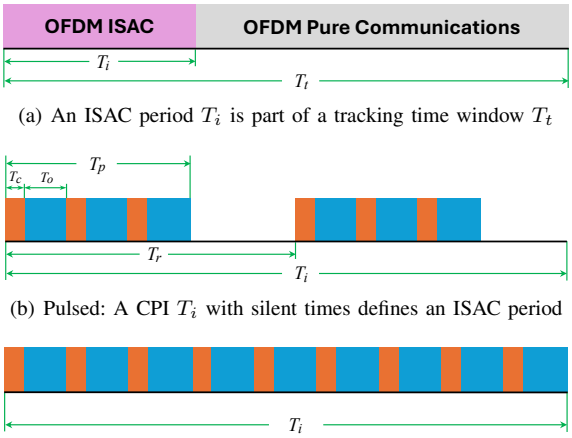
The proposed time structure of OFDM ISAC waveforms for PF-SLTR is shown in Fig. 2, which applies to every transmit antenna in MIMO. A target tracking period T_t, which is usually in dozens of milliseconds (ms; e.g., 25ms, 50ms), contains one ISAC period T_i to sense the moving ToI. Tens or hundreds of microseconds (μs) are, in practice, sufficient for an ISAC period. To save computing resources and without compromising the necessary accuracy of target tracking, there is no need to use the entire T_t time window for radar sensing. The remaining T_t-T_i seconds can be employed for pure communications to improve, e.g., throughput and reliability. Depending on how we use an MIMO-OFDM ISAC station, we can employ two types of waveform structures:

- **Pulsed Waveforms**: In this scheme, silent times are included between consecutive pulses. The transmit array and the receive array operate in either a time-division duplex or full-duplex manner, corresponding to the non-blind minimum round-trip delay of T_p or 0, respectively. During these silent times, the radar receiver can listen to *far* target echoes and resolve target parameters. This scheme is identical to that of the typical pulse-Doppler radars: The maximum detectable range is determined by the duration of the silence (i.e., T_r-T_p) in the time-division duplex mode or by the pulse repetition interval T_r in the full-duplex mode, where T_p is the pulse duration. Within each pulse duration, several OFDM symbols, together with their cyclic prefixes (CPs), are arranged back-to-back. This is a *sensing-centric* solution where the ranging capacity is improved by adding silent times and sacrificing the communications throughput.
- **Continuous-Wave (CW) Waveforms**: In this scheme, no silent times are contained between consecutive pulses. The transmit array and the receive array are supposed to be well isolated, and they operate in a full-duplex manner. The maximum resolvable range is determined by the length of the CP, which ensures that the *near* ToI can be treated as a scatterer. As a result, the CP length fully covers all possible path delays so that the circular convolution property is preserved for FFT-based signal processing, for example, frequency-domain channel estimation for communications and matched filtering for ranging. This is a *communications-centric* solution where the CP duration limits the ranging capacity, while the communication data streams remain unaffected.

Note that in the pulsed case, the circular convolution property is not inherently preserved for sensing signal processing, because the ToI, as a scatterer in the sensing channel, may not fall within the CP duration. Therefore, FFT-based frequency-domain methods require additional treatment compared to the CW case, as to be elaborated on in the following subsections. However, the scattering effect of the ToI may not impact the communication channel, since in the pulsed case, targets are typically far from the station, whereas communication users are located much closer. If the sensing ToI and communication users are both nearby, the CW scheme—where the CP can cover all path delays—should be adopted.

A. Pulsed MIMO-OFDM ISAC

In this mode, MIMO-OFDM ISAC works like a pulsed radar, and the only distinction is that the OFDM waveforms are employed at transmit antennas, instead of the canonical radar waveforms (e.g., phase-coded and chirp signals). Suppose that M OFDM symbols are included in each pulse, and the number of subcarriers in OFDM is N_c. We have $T_p=M\cdot(T_c+T_o)$ and $T_o=1/\Delta_f=N_c/B=N_cT_s$, where Δ_f is the subcarrier spacing. Let $\mathbf{c}_{p,m}(n)\in\mathbb{C}^{N_t}$ denote the constellation points



(a) An ISAC period T_i is part of a tracking time window T_t

(b) Pulsed: A CPI T_i with silent times defines an ISAC period

(c) CW: A CPI T_i without silent times defines an ISAC period

Fig. 2. The time structure of OFDM ISAC waveforms. Cyclic prefixes (CPs) are visualized by orange rectangles, while data payloads are indicated by blue rectangles. (b): pulsed OFDM ISAC waveforms; (c): continuous-wave (CW) OFDM ISAC waveforms. The tracking time period is T_t, and the ISAC period is T_i. For pulsed waveforms in (b), within a coherent processing interval (CPI) T_i, two pulses repeat with the pulse repetition interval (PRI) T_r. Each pulse has the time duration T_p. The silent time between two consecutive pulses is therefore $T_r - T_p$. Within each pulse, three CP-appended OFDM symbols are included; the duration of each OFDM symbol is T_o, whereas that of each CP is T_c. For CW waveforms in (c), we can treat $T_r = T_p$ so that no silent times are inserted. The Doppler processing for both structures is algorithmically similar.

on the n^{th} subcarrier in the p^{th} pulse and m^{th} OFDM symbol, where $p \in [N_p]$, $m \in [M]$, and $n \in [N_c]$. The time-domain waveform $\mathbf{s}_p(l)$ to be transmitted in the p^{th} pulse is

$$\mathbf{s}_p(l) = \begin{cases} \mathbf{s}_{p,\text{eff}}(l), & \textbf{if } 0 \le l \le \langle T_p/T_s \rangle - 1, \\ \mathbf{0}, & \textbf{if } \langle T_p/T_s \rangle \le l \le \langle T_r/T_s \rangle - 1, \end{cases} \tag{34}$$

where $\mathbf{s}_{p,\text{eff}}(l)$ for $0 \le lT_s \le T_p$ is the effective (i.e., non-zero) transmit waveform at the logical time l in the p^{th} pulse, consisting of M back-to-back CP-appended OFDM time-domain symbols; $\{\mathbf{s}_{p,\text{eff}}(l)\}_{l:\ 0\le l\le \langle T_p/T_s\rangle -1}$ is determined by $\{\mathbf{c}_{p,m}(n)\}_{\forall p\in[N_p],m\in[M],n\in[N_c]}$ via IFFT and CP addition; see, e.g., [14, Eq. (3)], [15, Eq. (2)], [13, Eq. (1)]. Note that within the time window $[T_p, T_r]$, the transmitter keeps silent. Note also that $N_{\text{cr}} \neq N_c$: the former is the FFT length of the whole transmit signal $\{\mathbf{s}_p(l)\}_{\forall l\in[L]}$ in which multiple CP-added OFDM symbols and a silent time slot are contained [cf. (5) and (27)], while the latter is the FFT length of one single CP-excluded OFDM symbol. In the practice of pulsed radars, $N_c \ll N_{\text{cr}} = L$.

The transmit MIMO-OFDM time-domain signals $\mathbf{s}_p$ defined in (34) are then propagated through the MIMO channel (4) and received by the radar receive array as $\{\mathbf{y}_p(l)\}_{\forall l\in[L]}$. The data evidence for a hypothesized ToI parameter pair $\boldsymbol{\varphi} := (\tau, \nu, \theta) \in \mathbb{R}^3$ is quantified by the cost functions in Methods 1 and 3, to be fed into the Gibbs-posterior-based PF-SLTR (15). If frequency-domain Methods 2 and 4 are to be used, FFT from $\{\mathbf{s}_p(l)\}_{\forall l\in[L]}$ to $\{\bar{\mathbf{s}}_p(n)\}_{\forall n\in[N_{\text{cr}}]}$ must be explicitly conducted *without removing CPs*, because the circular convolution property of FFT was destroyed, so that CPs are also part of effective sensing waveforms and $\{\bar{\mathbf{s}}_p(n)\}_{\forall n\in[N_{\text{cr}}]}$ do not equal $\{\mathbf{c}_{p,m}(n)\}_{\forall m\in[M],n\in[N_c]}$.

B. Continuous-Wave MIMO-OFDM ISAC

The pulse-Doppler radar signal processing can also be applied to CW MIMO-OFDM ISAC systems, just treating $T_r = T_p = M \cdot (T_c + T_o)$. Because we assumed that the maximum target round-trip delay is covered by the CP duration, the circular convolution property of the FFT can be preserved. As a result, efficient frequency-domain processing is applicable. To be specific, *after CP removal*, the MIMO channel propagation can be written as

$$\bar{\mathbf{y}}_{p,m}(n) = \beta_0 \boldsymbol{b}(\theta_0)\boldsymbol{a}^{\mathsf{H}}(\theta_0)\mathbf{c}_{p,m}(n)e^{-j2\pi n\Delta_f \tau_0}e^{j2\pi pT_r\nu_0} + \bar{\mathbf{n}}_{c,p,m}(n), \tag{35}$$

for every $p \in [N_p]$, $m \in [M]$, and $n \in [N_c]$ (not $[N_{\text{cr}}]$). Note that within the same pulse, the Doppler frequency shift is assumed to be constant so that the Doppler phase term $e^{j2\pi pT_r\nu_0}$ does not depend on m. Therefore, the data evidence for a hypothesized ToI parameter pair $\boldsymbol{\varphi} := (\tau, \nu, \theta) \in \mathbb{R}^3$ is quantified by the cost functions in frequency-domain Methods 2 and 4. Note that ρ_2 and ρ_4 need to be slightly modified to encompass the summations over $m \in [M]$ and $n \in [N_c]$:

$$\rho_2'(\boldsymbol{y}, \boldsymbol{\varphi}) := \min_{\gamma\in\mathbb{C}} \sum_{p=0}^{N_p-1}\sum_{m=0}^{M-1}\sum_{n=0}^{N_c-1} \left\| \bar{\boldsymbol{y}}_{p,m}(n) - \gamma \boldsymbol{b}(\theta)\boldsymbol{a}^{\mathsf{H}}(\theta)\mathbf{c}_{p,m}(n)e^{-j2\pi n\Delta_f\tau}e^{j2\pi pT_r\nu} \right\|_2^2, \tag{36}$$

and

$$\rho_4'(\boldsymbol{y}, \boldsymbol{\varphi}) := -\ln \left[\left| \sum_{p=0}^{N_p-1}\sum_{m=0}^{M-1}\sum_{n=0}^{N_c-1} \bar{\boldsymbol{y}}_{p,m}^{\mathsf{H}}(n)\boldsymbol{b}(\theta)\boldsymbol{a}^{\mathsf{H}}(\theta)\mathbf{c}_{p,m}(n)e^{-j2\pi n\Delta_f\tau}e^{j2\pi pT_r\nu} \right|^2 \right]. \tag{37}$$

Numerically evaluating (36) and (37) in the frequency domain, especially when the FFT technique is applied, can be significantly faster than evaluating (19) and (25) in the time domain. This highlights the computational benefit of the CW MIMO-OFDM ISAC systems, however, coming with a limited ranging capability set by the CP duration. In contrast, pulsed MIMO-OFDM ISAC systems can support much larger ranging regions without considering the time length of CPs, however, at the cost of a higher computational burden[4] and lower communications throughput.

C. Overall PF-SLTR Algorithm

In this section, we summarize the PF-SLTR for MIMO-OFDM ISAC systems in Algorithm 1, which is adapted from the canonical particle filter for dynamic systems (1); see [38, Algorithm 4], [37, p. 468]. Some algorithmic details and operational remarks, such as the basics of particle filtering and the notions of resampling and effective sample size, can be seen in [38], [37, Chap. 15], [39]. For extensive discussions on PF-SLTR, see Section V.

[4]Although this burden can be algorithmically reduced by FFT tricks; cf. (25) and (27); NB: in practice, $MN_c \le N_{\text{cr}}$ and $N_c \ll N_{\text{cr}}$.

Algorithm 1 PF-SLTR in MIMO-OFDM ISAC

Definition: k is the discrete tracking-time index; N_{par} is the number of state particles; $\boldsymbol{x}_{k,i}$ is the posterior state particles at k and $u_{k,i}$ the associated weights, $\forall i \in [N_{\text{par}}]$; $\boldsymbol{\varphi}_{k,i}$ is the range-Doppler-angle representation of $\boldsymbol{x}_{k,i}$; N_{eff} is the effective sample size and N_{thres} its threshold.

Remark: For illustration and computational efficiency, we only show frequency-domain processing using (27) and (37). In addition, we suppose that $\hat{\boldsymbol{R}}_s := P_t \boldsymbol{I}_{N_t}$; otherwise, cost functions can be modified by incorporating denominators as in (23) and (24).

Initialization: N_{par}, N_{thres}, ξ, and $\{\boldsymbol{x}_{0,i}, u_{0,i}\}_{i\in[N_{\text{par}}]}$.

Input: Radar received signals $\boldsymbol{y}_k,\ k = 1, 2, 3, ...$; see (6)

// Step 1: Generate Prior State Particles; See (1)
for $i = 0 : N_{\text{par}} - 1$ **do**
  Sample $\boldsymbol{w}_{k-1,i}$ from the distribution of $\mathbf{w}_{k-1}$
  $\boldsymbol{x}_{k,i} \leftarrow \boldsymbol{f}_k(\boldsymbol{x}_{k-1,i}, \boldsymbol{w}_{k-1,i})$
  Translate $\boldsymbol{x}_{k,i}$ to $\boldsymbol{\varphi}_{k,i}$ using geometric relations
  $\eta_{k,i} \leftarrow u_{k-1,i}$
end for
// Step 2: Evaluate $\boldsymbol{y}_k$-Data Evidence for Every $\boldsymbol{\varphi}_{k,i}$
for $i = 0 : N_{\text{par}} - 1$ **do**
  if Pulsed Scheme **then**
    Calculate cost $\rho(\boldsymbol{y}_k, \boldsymbol{\varphi}_{k,i})$ using (27)
  else if CW Scheme **then**
    Calculate cost $\rho(\boldsymbol{y}_k, \boldsymbol{\varphi}_{k,i})$ using (37)
  end if
end for
// Step 3: Generate Posterior Particles $\boldsymbol{x}_{k,i}$; See (15)
for $i = 0 : N_{\text{par}} - 1$ **do**
  Keep $\boldsymbol{x}_{k,i}$ unchanged
  Update weight by $u_{k,i} \leftarrow \eta_{k,i} \cdot e^{-\xi\rho(\boldsymbol{y}_k, \boldsymbol{\varphi}_{k,i})}$
end for
Normalize weights $\{u_{k,i}\}_{\forall i\in[N_{\text{par}}]}$
// Step 4: Resampling
$N_{\text{eff}} \leftarrow 1/\sum_{i=0}^{N_{\text{par}}-1} u_{k,i}^2$
if $N_{\text{eff}} < N_{\text{thres}}$ **then**
  Resample N_{par} times from $\{\boldsymbol{x}_{k,i}, u_{k,i}\}_{\forall i\in[N_{\text{par}}]}$
  $u_{k,i} \leftarrow 1/N_{\text{par}},\ \forall i \in [N_{\text{par}}]$
end if

Output: Posterior particles and weights $\{\boldsymbol{x}_{k,i}, u_{k,i}\}_{\forall i\in[N_{\text{par}}]}$.

The computational complexity, in time, of PF-SLTR can be analyzed as follows:

- In Step 1, if $\boldsymbol{f}_k$ is linear in $\mathbf{x}_{k-1}$, which is the case for the usual constant-velocity and constant-acceleration models [35], the complexity is $\mathcal{O}(N_{\text{par}} d_x^2)$, where d_x denotes the dimension of $\mathbf{x}_{k-1}$ (assuming fixed across different k's).
- In Step 2, for the pulsed scheme, the complexity is $\mathcal{O}(N_{\text{par}} N_p N_{\text{cr}}(N_t + N_r))$; for the CW scheme, the complexity is $\mathcal{O}(N_{\text{par}} N_p M N_c(N_t + N_r))$.
- In Step 3, the complexity is $\mathcal{O}(N_{\text{par}})$ because the $\boldsymbol{y}_k$-data evidence $\{\rho(\boldsymbol{y}_k, \boldsymbol{\varphi}_{k,i})\}_{\forall i\in[N_{\text{par}}]}$ of the particles have already been evaluated in Step 2.
- In Step 4, the complexity is $\mathcal{O}(N_{\text{par}})$, if the systematic resampling is adopted.

Overall, the computational complexity in time of PF-SLTR is $\mathcal{O}(N_{\text{par}} d_x^2 + N_{\text{par}} N_p N_{\text{cr}}(N_t + N_r))$ for the pulsed scheme, and is $\mathcal{O}(N_{\text{par}} d_x^2 + N_{\text{par}} N_p M N_c(N_t + N_r))$ for the CW scheme.

V. Discussions on PF-SLTR

In this section, we discuss the assumptions, advantages, and limitations of PF-SLTR.

State Estimation: In Bayesian target tracking, target existence detection, track initialization, and state estimation are related but distinct inference tasks. This article assumes that the ToI is present in the surveillance region and that track initialization has already been performed. This assumption is standard in the target tracking literature when the objective is to evaluate the performance of a state estimation algorithm in isolation [35], [44], i.e., to demonstrate that the proposed particle filtering mechanism yields more accurate and stable state estimates under raw radar measurements. Therefore, we specifically focus on the recursive Bayesian estimation of the target kinematic state $\mathbf{x}_k$ from raw radar measurements $\mathbf{y}_k$; recall (1) and (6). Note that operating directly on raw radar measurements does not require the target-existence decision to be jointly considered; see, e.g., [36], [40], [41], [46].

Existence Detection: When target tracking considers existence detection, track-before-detect particle filtering (TBD PF) is standard [47], [48], [62]. However, TBD PF relies heavily on the accuracy of the likelihood model $q(\boldsymbol{y}_k|\boldsymbol{\varphi}_k, e_k = 1)$ and the IPN model $q(\boldsymbol{y}_k|e_k = 0)$, where $\boldsymbol{y}_k$ denotes the radar raw data at time k [see (6)], $\boldsymbol{\varphi}_k$ defines the ToI parameter [see (9)], and e_k is a Boolean that equals one if the ToI presents and zero otherwise. In the radar target tracking literature (e.g., TBD PF), these two probabilistic models are typically constructed using simplified assumptions (e.g., Gaussian IPN, single radio path, or single target), which may be inaccurate under realistic conditions such as dense multipath, multiple targets, or non-Gaussian interference. To be specific, when there exist scatterers (including targets of non-interest) and the statistics of these scatterers are unknown, the measurement model $q(\boldsymbol{y}_k|\boldsymbol{\varphi}_k, e_k = 1)$ and the IPN model $q(\boldsymbol{y}_k|e_k = 0)$ may deviate from Gaussianity, since the IPN term $\mathbf{n}_c(t)$ in (3) is generally non-Gaussian; cf. (2). This particularly affects signal-level particle filters that rely on explicit likelihood evaluation, for example, those that assume the Gaussianity of the IPN $\mathbf{n}_c(t)$. Consequently, TBD PF remains sensitive to likelihood model mismatch, particularly in challenging environments where accurate probabilistic modeling and statistical characterization of the measurements are difficult. Hence, existence detection using TBD PF is not considered.

Multi-Target Tracking: Extending the proposed PF-SLTR framework to the multi-target tracking setting is not a straightforward generalization, as it introduces several nontrivial challenges that are fundamentally different in nature from the single-target case. In particular, the following three difficulties are immediate [63]–[65]: a) data association that determines which path component of the raw measurement $\mathbf{y}_k$ is generated by which target [cf. (2), (3), and (6)]; b) track management that includes targets' initiation and termination; and c) IPN modeling where the IPN $\mathbf{n}_c(t)$ depends on other targets'

parameters. Handling these technical aspects typically requires a different modeling paradigm, such as Random Finite Set (RFS)-based formulations, and would significantly increase the scope and complexity of the problem. For this reason, and consistent with common practice in the development of new filtering methodologies, we restrict attention to the single-target case and assume that the ToI has already been initialized. On the other hand, it is worth noting that the proposed PF-SLTR can be extended to multi-target tracking. To be specific, it can be incorporated into existing multi-target Bayesian frameworks by replacing the state- and measurement-update steps for each target with the proposed PF-SLTR, particularly when data association and track management are handled separately. The benefit is that, unlike conventional PF and TBD PF methods, PF-SLTR does not explicitly require the accurate modeling of the IPN $\mathbf{n}_c(t)$: recall that in Algorithm 1, the cost functions (27) and (37) do not rely on $\mathbf{n}_c(t)$. For example, supposing we have two targets in the surveillance region and no other scatterers exist, (2) simplifies into

$$\begin{aligned}\mathbf{y}(t) \quad &= \beta_1 \boldsymbol{b}(\theta_1)\boldsymbol{a}^{\mathsf{H}}(\theta_1)\mathbf{s}(t-\tau_1)e^{j2\pi\nu_1 t}+ \\ &\quad \beta_2 \boldsymbol{b}(\theta_2)\boldsymbol{a}^{\mathsf{H}}(\theta_2)\mathbf{s}(t-\tau_2)e^{j2\pi\nu_2 t}+\mathbf{n}(t),\end{aligned} \tag{38}$$

where $(\tau_1, \nu_1, \theta_1)$ denotes the parameter of the first target, $(\tau_2, \nu_2, \theta_2)$ that of the second target, and $\mathbf{n}(t)$ the Gaussian environmental noise. When we track the first target, the radar measurement model becomes

$$\mathbf{y}(t) \quad = \beta_1 \boldsymbol{b}(\theta_1)\boldsymbol{a}^{\mathsf{H}}(\theta_1)\mathbf{s}(t-\tau_1)e^{j2\pi\nu_1 t}+\mathbf{n}_c(t), \tag{39}$$

where the IPN term $\mathbf{n}_c(t) \coloneqq \beta_2 \boldsymbol{b}(\theta_2)\boldsymbol{a}^{\mathsf{H}}(\theta_2)\mathbf{s}(t-\tau_2)e^{j2\pi\nu_2 t}+\mathbf{n}(t)$. Instead, when we track the second target, the radar measurement model becomes

$$\mathbf{y}(t) \quad = \beta_2 \boldsymbol{b}(\theta_2)\boldsymbol{a}^{\mathsf{H}}(\theta_2)\mathbf{s}(t-\tau_2)e^{j2\pi\nu_2 t}+\mathbf{n}_c(t), \tag{40}$$

where the IPN term $\mathbf{n}_c(t) \coloneqq \beta_1 \boldsymbol{b}(\theta_1)\boldsymbol{a}^{\mathsf{H}}(\theta_1)\mathbf{s}(t-\tau_1)e^{j2\pi\nu_1 t}+\mathbf{n}(t)$. As indicated, when data association and track management are handled separately, which is a common practice, multi-target tracking can be decomposed into a set of single-target tracking problems: Different targets are to be tracked by separate particle filters. Therefore, within the context of target tracking using MIMO-OFDM radar without explicit IPN handling, focusing on single-target state estimation does not compromise the technical contributions of this article.

Applicability of PF-SLTR: Below, we compare the proposed PF-SLTR with the conventional likelihood-based PF and TBD PF, under various operating conditions. All three frameworks are formulated at the signal level; namely, they process raw radar data $\mathbf{y}_k$ directly [see (6)], rather than extracted range–Doppler–angle measurements of $(\tau_{0,k}, \nu_{0,k}, \theta_{0,k})$. Typically, the following conditions are investigated.

- *Large Data Dimensions in Time, Frequency, and Space*: When the transmit antenna number N_t, receive antenna number N_r, bandwidth B, or CPI length T_i are large, extracting range-Doppler-angle measurements via matched filtering or advanced optimization becomes computationally intensive. This makes information-level tracking pipelines (i.e., detect-then-track) computationally expensive, especially when combined with particle filtering. In such cases, signal-level approaches (e.g., PF-SLTR) are preferred to reduce computational burden.
- *Model Mismatch in Likelihood Function* $\boldsymbol{\varphi}_k \mapsto q(\boldsymbol{y}_k \mid \boldsymbol{\varphi}_k)$: The performance of the conventional likelihood-based PF and TBD PF relies heavily on the accuracy of the likelihood model $q(\boldsymbol{y}_k \mid \boldsymbol{\varphi}_k)$. If non-negligible mismatches exist in $q(\boldsymbol{y}_k \mid \boldsymbol{\varphi}_k)$, PF-SLTR can be considered first since it does not mandate the accurate modeling of the IPN term $\mathbf{n}_c(t)$ and the likelihood relation $q(\boldsymbol{y}_k \mid \boldsymbol{\varphi}_k)$, whereas the likelihood-based PF and TBD PF do.
- *Low Signal-to-Interference-Plus-Noise Ratio (SINR)*: When the received ToI signal is weak relative to IPN, TBD PF is generally preferred, provided that the measurement model $q(\boldsymbol{y}_k|\boldsymbol{\varphi}_k, e_k = 1)$ and the IPN model $q(\boldsymbol{y}_k|e_k = 0)$ can be accurately specified. However, the performance of TBD PF is highly sensitive to the errors in the likelihood and IPN models. Therefore, when a significant model mismatch is present, PF-SLTR can be preferable across different SINR regimes.
- *Dense Clutter (Due to Targets of Non-Interest and Scatterers)*: Dense clutter complicates IPN modeling (i.e., determining the statistical properties of $\mathbf{n}_c(t)$), leading to likelihood mismatch and degraded performance of likelihood-based and TBD PF methods. In contrast, PF-SLTR tends to be more robust in such scenarios because it avoids explicit likelihood and IPN modeling.
- *Fast-Fading (i.e., Rapidly Varying Path Gains* $\beta_{0,k}$*)*: Standard Bayesian filtering frameworks require augmenting nuisance parameters, such as complex path gains $\beta_{0,k}$, into the state vector, increasing its dimensionality and thus degrading statistical and computational efficiency. When these parameters vary abruptly across tracking periods k, standard state-transition models (e.g., random walk or constant-velocity) become ineffective. Consequently, likelihood-based PF (including the variant Rao-Blackwellized PF) and TBD PF methods become less effective. In contrast, PF-SLTR does not explicitly model path gains and is therefore robust to their rapid variations.

In summary, likelihood-based PF is most effective when accurate statistical models are available and the state dimension is moderate. TBD PF methods are advantageous in low-SINR regimes when reliable likelihood models can be constructed. The proposed PF-SLTR is particularly beneficial in scenarios involving significant model uncertainty or rapidly varying path-gain parameters where explicit likelihood modeling becomes unreliable or computationally burdensome.

Cost Functions: In this article, the cost functions ρ_3 in (25), ρ_4 in (27), and ρ_4' in (37) are studied and recommended; see Algorithm 1. This choice is motivated by the minimization-based marginalization trick in (19) and (21), which handles the nuisance parameter β_0; cf. Propositions 1 and 2. For all radars operating under the measurement model (2) [see also (3)-(6)], the cost functions designed in (25), (27), and (37) are applicable within the proposed PF-SLTR framework, regardless of the waveform structure or parameterization of the wireless signal $\mathbf{s}(t)$ and noise $\mathbf{n}(t)$. Specifically, ρ_3 in (25) can be adopted when time-domain processing is employed for

pulsed radars, ρ_4 in (27) when frequency-domain processing is used for pulsed radars, and ρ_4' in (37) when frequency-domain processing is applied to continuous-wave OFDM radars. Given that the radar measurement model (2) is general, the proposed PF-SLTR in Algorithm 1, equipped with the cost functions ρ_3, ρ_4, or ρ_4', is broadly applicable to a wide range of MIMO radar systems, including both conventional radars and ISAC radars. In this article, MIMO-OFDM communication stations serve as radars, as raw OFDM communication waveforms are reused for sensing. Indeed, other types of cost functions may also be developed, provided that they comply with the fundamental rule in Rule 1. However, discovering these new cost functions, derived from alternative motivations, can be explored in future research. As an initiating article in this research direction, focusing on the proposed ρ_3, ρ_4, and ρ_4' does not compromise the technical contributions of this article and the general applicability of the proposed PF-SLTR algorithm.

Likelihood Adaptation: In the literature, such as [66, Algo. 1], learning the likelihood relation $\boldsymbol{x}_k \mapsto q(\boldsymbol{y}_k|\boldsymbol{x}_k)$ from historical data pairs $(\boldsymbol{y}_k, \boldsymbol{x}_k)$ is suggested; cf. (1). Within the problem setting of this article, adapting this idea would require constructing or learning the likelihood relation $\boldsymbol{\varphi}_k \mapsto q(\boldsymbol{y}_k|\boldsymbol{\varphi}_k)$ associated with the raw radar measurement $\boldsymbol{y}_k$ and the target parameter $\boldsymbol{\varphi}_k \coloneqq (\tau_{0,k}, \nu_{0,k}, \theta_{0,k})$. This is difficult for the following three reasons:

- The required labeled training data pairs $(\boldsymbol{y}_k, \boldsymbol{\varphi}_k)$ are generally unavailable in online radar target tracking problems. Data collected from other scenarios may not ensure sufficient cross-scenario generalizability because the radio propagation environment and scatterer (including targets of no interest) conditions can change significantly from scenario to scenario.
- The signal-level measurement $\boldsymbol{y}_k$ is high-dimensional in MIMO pulse-Doppler radar systems, as it may contain samples across receive antennas, fast-time range bins, slow-time Doppler bins, OFDM symbols, and subcarriers; cf. (4), (5), (35), and (6). Hence, learning a reliable likelihood relation $\boldsymbol{\varphi}_k \mapsto q(\boldsymbol{y}_k|\boldsymbol{\varphi}_k)$ in such high-dimensional spaces would require substantial training data and computational resources, which is difficult to support within a short tracking period T_t; cf. Fig. 2.
- The likelihood relation may vary across tracking periods k because nuisance parameters and IPN statistics can be time-varying. In particular, the ToI path gain $\beta_{0,k}$ may change rapidly across different tracking periods k, and the IPN term may also evolve with time-varying scatterers. Therefore, a likelihood model learned in one period or scenario may not remain valid in another.

For these difficulties, [66] assumes an off-line training phase in which a likelihood-like relation is learned from sufficient training data, and this learned relation is assumed to remain valid in the online deployment scenarios. To relax this assumption, this article takes a different route. Instead of learning or adapting the explicit likelihood relation $\boldsymbol{\varphi}_k \mapsto q(\boldsymbol{y}_k|\boldsymbol{\varphi}_k)$, PF-SLTR uses domain-motivated data-evidence cost functions within a Gibbs-posterior particle filtering framework.

VI. Experiments

In this section, we use experiments to validate the efficiency of the proposed PF-SLTR (i.e., Algorithm 1) in MIMO-OFDM ISAC systems. Let the state vector $\mathbf{x}_k \coloneqq [R_k, \varsigma_k, \theta_k, \omega_k]^\mathsf{T}$ contain the ToI range R_k, radial speed ς_k, DoA angle θ_k, and DoA angular velocity ω_k.

For the state transition equation $\mathbf{x}_k = \boldsymbol{f}_k(\mathbf{x}_{k-1}, \mathbf{w}_{k-1})$ in (1), we use the constant-velocity (CV) model [35, Eq. (14)], which is linear in $\mathbf{x}_k$, because the CV model naturally captures the kinematic relations that the radial speed and DoA angular velocity are the time derivatives of the range and DoA angle, respectively. We have

$$\mathbf{x}_k = \mathrm{diag}(\boldsymbol{F}_{k-1}, \boldsymbol{F}_{k-1})\mathbf{x}_{k-1} + \mathrm{diag}(\boldsymbol{G}_{k-1}, \boldsymbol{G}_{k-1})\mathbf{w}_{k-1}, \tag{41}$$

where diag forms a block-diagonal matrix from its arguments,

$$\boldsymbol{F}_{k-1} \coloneqq \begin{bmatrix} 1 & T_t \\ 0 & 1 \end{bmatrix}, \text{ and } \boldsymbol{G}_{k-1} \coloneqq \begin{bmatrix} T_t^2/2 \\ T_t \end{bmatrix}.$$

For the measurement model $\mathbf{y}_k = \boldsymbol{h}_k(\mathbf{x}_k, \mathbf{v}_k)$ in (1), it particularizes into (4) in the time domain, (5) in the frequency domain, or (35) for the CW MIMO-OFDM case. Since this measurement mechanism is nonlinear in $\mathbf{x}_k$, linear state estimation approaches, such as Kalman filtering, are not applicable. In addition, because the nonlinearity is severe, nonlinear Kalman variants, e.g., extended and unscented Kalman filtering, often lead to unreliable estimates [37, p. 433, p. 462]. Therefore, particle filtering is widely adopted in the literature of signal-level target tracking; see, e.g., [34, Figs. 4-5], [36], [40], [41]. However, employing conventional particle filters requires additional modeling assumptions due to the unknown statistical information of the IPN terms $\mathbf{n}_{c,p}(l)$, $\bar{\mathbf{n}}_{c,p}(n)$, and $\bar{\mathbf{n}}_{c,p,m}(n)$ in (4), (5), and (35), respectively.

The following filtering schemes are implemented for performance comparison.

KF-ILTR: Kalman filtering (KF) for information-level target tracking (ILTR). First, we obtain the measurements of $(\tau_0, \nu_0, \theta_0)$ at each tracking time k, using the 3-dimensional (3D) range-Doppler-DoA matched filter. For demonstration purposes only, other advanced methods, e.g., [16], [25], [26], [49, Table II], are not implemented because they are even more computationally prohibitive for real-time use (e.g., within the tracking time window $T_t = 50$ms). The computational complexity, in time, of the 3D range-Doppler-DoA matched filters (27) and (37) is $\mathcal{O}(N_{\text{tg}}^3 N_p N_{\text{cr}}(N_t + N_r))$ and $\mathcal{O}(N_{\text{tg}}^3 N_p M N_{\text{c}}(N_t + N_r))$, respectively, where N_{tg} is the length of the tracking gate in each dimension. To clarify, to search for the peak of the matched filter output in a $N_{\text{tg}} \times N_{\text{tg}} \times N_{\text{tg}}$ grid of range-Doppler-DoA, we need to evaluate the ambiguity function (27) or (37) N_{tg}^3 times. As indicated, even $N_{\text{tg}} = 30$, we need to evaluate ambiguity functions 27000 times, and the complexity of each time is $\mathcal{O}(N_p N_{\text{cr}}(N_t + N_r))$ or $\mathcal{O}(N_p M N_{\text{c}}(N_t + N_r))$. For systems with large N_p, N_{cr} (i.e., L), M, N_c, N_t, and N_r, even the traditional 3D range-Doppler-DoA matched filtering is unaffordable, no mention

advanced approaches [25], [26], [49, Table II]. In this case, the measurement model $\mathbf{y}_k = \boldsymbol{h}_k(\mathbf{x}_k, \mathbf{v}_k)$ in (1) simplifies to

$$\mathbf{y}_k = \begin{bmatrix} 1 & 0 & 0 & 0 \\ 0 & 1 & 0 & 0 \\ 0 & 0 & 1 & 0 \end{bmatrix} \mathbf{x}_k + \mathbf{v}_k, \tag{42}$$

where $\mathbf{y}_k$ contains the measured values of the range $\bar{R}_k$, the radial velocity $\bar{\varsigma}_k$, and the DoA $\bar{\theta}_k$ that are calculated using the matched-filter estimates of $(\tau_0, \nu_0, \theta_0)$. Since both the state transition equation (41) and state measurement equation (42) are linear, Kalman filtering is applicable.

UKF-SLTR-A: The unscented Kalman filtering (UKF) for signal-level target tracking (SLTR) that augments (A) the real and imaginary components of the complex gain $\beta_{0,k}$ (due to the ToI) into the state vector $\mathbf{x}_k$ [37, Sec. 14.3]. In this case, the state measurement model is (4), (5), or (35). Because we do not know the statistical information of the IPN terms $\mathbf{n}_{c,p}(l)$, $\bar{\mathbf{n}}_{c,p}(n)$, and $\bar{\mathbf{n}}_{c,p,m}(n)$, it is assumed that the conditional distribution $q(\boldsymbol{y}_k|\boldsymbol{x}_k)$ is complex Gaussian and there are no scatterers. To be specific, at the tracking time k, for every p, m, n, we have

$$q(\bar{\boldsymbol{y}}_{k,p}(n)|\beta_0, \tau_0, \nu_0, \theta_0) \coloneqq \mathcal{CN}(\boldsymbol{\epsilon}_1,\ \sigma_{\text{cn}}^2 \boldsymbol{I}_{N_r}) \tag{43}$$

where $\boldsymbol{\epsilon}_1 \coloneqq \beta_0 \boldsymbol{b}(\theta_0)\boldsymbol{a}^{\mathsf{H}}(\theta_0)\bar{\mathbf{s}}_p(n)e^{-j2\pi n\Delta\tau_0}e^{j2\pi pT_r\nu_0}$, for the pulsed MIMO-OFDM paradigm [see (5)], or

$$q(\bar{\boldsymbol{y}}_{k,p,m}(n)|\beta_0, \tau_0, \nu_0, \theta_0) \coloneqq \mathcal{CN}(\boldsymbol{\epsilon}_2,\ \sigma_{\text{cn}}^2 \boldsymbol{I}_{N_r}) \tag{44}$$

where $\boldsymbol{\epsilon}_2 \coloneqq \beta_0 \boldsymbol{b}(\theta_0)\boldsymbol{a}^{\mathsf{H}}(\theta_0)\mathbf{c}_{p,m}(n)e^{-j2\pi n\Delta_f\tau_0}e^{j2\pi pT_r\nu_0}$ for the CW MIMO-OFDM paradigm [see (35)]; $\mathcal{CN}(\boldsymbol{\epsilon},\ \sigma_{\text{cn}}^2 \boldsymbol{I}_{N_r})$ denotes the complex Gaussian distribution with mean $\boldsymbol{\epsilon}$, covariance $\sigma_{\text{cn}}^2 \boldsymbol{I}_{N_r}$, and zero pseudo-covariance; σ_{cn}^2 is the assumed-known power of the channel noise. Since the measurement model is severely nonlinear in $\mathbf{x}_k$ (see the definitions of $\boldsymbol{\epsilon}_1$ and $\boldsymbol{\epsilon}_2$ above) and the likelihood models (43) and (44) can be misleading, the UKF-SLTR-A often gives unreliable state estimates [37, p. 462].

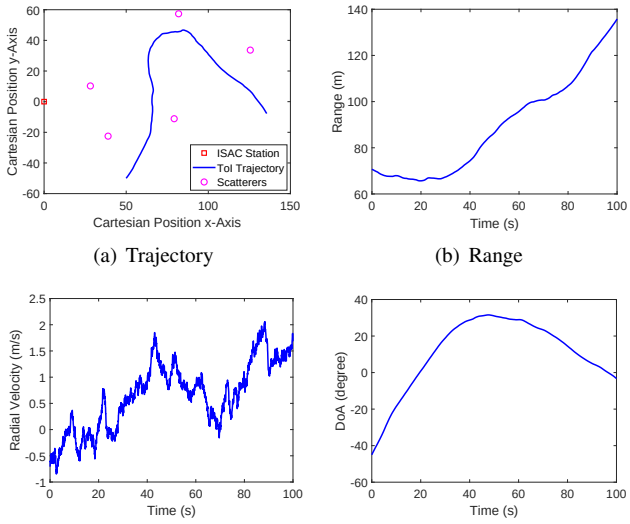
PF-SLTR-A: The traditional particle filtering (PF) for signal-level target tracking (SLTR) that augments (A) the real and imaginary components of the complex gain $\beta_{0,k}$ (due to the ToI) into the state vector $\mathbf{x}_k$ [36], [40], [41]. In this case, the UKF is replaced with the traditional PF and the remaining settings, e.g., the likelihood models (43) and (44), remain unchanged. As is frequently observed in practice, the convergence of PF-SLTR-A is difficult to ensure, especially when the path gain $\beta_{0,k}$ is significantly time-varying across different k's or when scatterers exist, which makes the likelihoods in (43) and (44) largely unreliable.

RBPF-SLTR-A: The Rao-Blackwellized particle filtering (RBPF) [52] for signal-level target tracking (SLTR) that augments (A) the real and imaginary components of the complex gain $\beta_{0,k}$ into the state vector $\mathbf{x}_k$. Since the state transition equation is linear in $\mathbf{x}_{k-1}$ and the measurement equation (2) [cf. (4) and (5)] is linear in $\beta_{0,k}$, the RBPF that marginalizes out $\beta_{0,k}$ using a Kalman filter can improve the statistical and computational efficiency, compared to the traditional PF-SLTR-A; see [53, Sec. II-G].

The performance of each method is measured by both the running times and the target-tracking mean-squared errors (MSEs). The experiments were performed in MATLAB R2025b on a Lenovo desktop with an Intel© Core™ i7-14700F processor (2.10 GHz), 64 GB of RAM, and a 64-bit operating system. All the source data and codes are available online at GitHub: https://github.com/Spratm-Asleaf/PF-SLTR-MIMO-OFDM.

In this section, we consider a continuous-wave MIMO-OFDM ISAC system with center frequency $f_c = 10$GHz for tracking a near and slow ToI. For supplementary experiments (e.g., the pulsed case for far and fast targets), see Appendix D in the online supplementary materials.

The experimental scenario is displayed in Fig. 3. Therein, the ToI is moving along a curved trajectory, and five static scatterers are assumed, with ranges $[30, 45, 100, 80, 130]$ and DoAs $[20, -30, 35, -8, 15]$, respectively. The communication-centric waveform structure in Fig. 2(c) is used, and the cost function in (37) is employed in PF-SLTR to track the ToI. For communications waveforms, we assume that each OFDM subcarrier contains random symbols uniformly from the quadrature amplitude modulation (QAM) constellation of order 64. Since during target tracking, the communication infrastructure and waveforms are reused for sensing, the communication performance remains unaffected.



(a) Trajectory (b) Range

(c) Radial Velocity (d) DoA

Fig. 3. Tracking the maneuvering ToI using CW MIMO-OFDM ISAC.

On the sensing side, the tracking time period is set to $T_t = 50$ms, and the total tracking time is 100s. To cover the maximum range of 150m, we let the CP duration be $T_c = 1\mu$s. Suppose that the OFDM symbol duration (for data payloads) is five times of the CP length (i.e., $T_o = 5\mu$s), the number of OFDM symbols in a pulse is $M = 1$, the number of subcarriers is $N_c = 256$, the number of transmit antennas is $N_t = 64$, the number of receive antennas is $N_r = 64$, and the number of pulses in a coherent processing interval is $N_p = 1$. Since using only the range and DoA information to track the ToI is sufficient, it is safe to set $N_p = 1$. As a result, the pulse duration is $T_p = M(T_c + T_o) = 6\mu$s, the pulse repetition

interval is $T_r = T_p = 6\mu$s, the coherent processing interval is $T_i = N_p T_r = 6\mu$s, the subcarrier spacing is $\Delta_f = 1/T_o = 0.2$MHz, the bandwidth is $B = N_c\Delta_f = 51.2$MHz, the sampling time interval and the round-trip delay resolution is $T_s = 1/B = 0.019531\mu$s (i.e., the range resolution is 2.93m), the resolution of sin-DoA (not DoA itself) is $2/64 = 1/32$. Let the normalized channel noise power be $\sigma_{\text{cn}}^2 \coloneqq 1$ and the transmit SNR (SNR_{tx}) be -10dB, where

$$\text{SNR}_{\text{tx}} \coloneqq 10\log_{10}(P_t/\sigma_{\text{cn}}^2). \tag{45}$$

The ToI path gain, normalized with respect to the initial ToI range $R_{0,0}$, is modeled as

$$\beta_{0,k} \coloneqq \kappa \cdot \left(\frac{R_{0,0}}{R_{0,k}}\right)^2 \cdot \sqrt{\text{s}_{0,k}} e^{j2\pi \text{r}_k}, \tag{46}$$

where κ denotes the attenuation factor at the initial range $R_{0,0}$ and $R_{0,k}$ the ToI range at tracking period k; $\text{s}_{0,k}$ follows the exponential distribution with unit mean, and r_k is uniformly distributed over $[0, 1]$; $\text{s}_{0,k}$ models the normalized Swerling-I-type radar-cross-section fluctuation of the ToI, while $e^{j2\pi \text{r}_k}$ models its random scattering phase [5, Chap. 2]. The factor $(R_{0,0}/R_{0,k})^2$ models the relative range-dependent amplitude attenuation. The receive SNR is determined by the transmit SNR and the path gain $\beta_{0,k}$ through (2). Both the real and imaginary components of $\beta_{0,k}$ vary abruptly across tracking periods k. In the experiments, we set $\kappa \coloneqq 0.7$. Moreover, the number of particles is set to $N_{\text{par}} \coloneqq 200$, the effective particle number used in particle resampling is $N_{\text{thres}} \coloneqq N_{\text{par}}/2$, and the power coefficient in (15) is $\xi \coloneqq 1$.

The tracking results for the 2-dimensional (2D) Cartesian positions (calculated using tracked ranges and DoAs) are shown in Table I and Appendix D in the online supplementary materials. In Table I, the 2D position MSEs are averaged over all different k's and independent Monte-Carlo (MC) trials, so are the running times (Time); however, we found that the empirical performance variations are not obvious across different MC episodes because MSEs are averaged on a long time trajectory indexed by k. From Table I, we can see that PF-SLTR is *significantly* better than KF-ILTR, UKF-SLTR-A, PF-SLTR-A, and RBPF-SLTR-A, in terms of both computation and accuracy. This is because KF-ILTR must consume a huge amount of time to obtain the raw measurements of the ToI parameters $(\tau_{0,k}, \theta_{0,k})$ at each time k; NB: when $N_p = 1$, Doppler processing is disabled. Within a tracking time window of $T_t = 50$ms, spending 89.3ms on computations is operationally intolerable because target tracking is a real-time signal processing problem. In contrast, the proposed PF-SLTR does not require this operation. In addition, the convergence of UKF-SLTR-A, PF-SLTR-A, and RBPF-SLTR-A is difficult to ensure for the following two reasons: First, it is challenging to accurately track the quickly-jumping path gain $\beta_{0,k}$ in (46);[5] second, the likelihood functions in (43) and (44) are not sufficiently precise due to the presence of unknown scatterers. However, the proposed PF-SLTR in Algorithm 1 does not require estimating $\beta_{0,k}$ or relying on the exact likelihood function, resulting in superior performance.

[5]Under the model (46), both the real and imaginary components of $\beta_{0,k}$ vary abruptly across tracking periods k.

TABLE I
TRACKING RESULTS FOR THE SCENARIO IN FIG. 3

	PF-SLTR	KF-ILTR	UKF-SLTR-A	PF-SLTR-A	RBPF-SLTR-A
MSE	**0.0070**	1.5520	(Diverged)	(Diverged)	(Diverged)
Time	**29.2**	89.3	1.3	32.4	30.1

Note: Unit for MSE: m^2; unit for Time: ms.

In the following, we present the tracking results of PF-SLTR under different parameters. Results of other filters are not displayed because, as we can see, they are significantly dominated by PF-SLTR. When we vary one parameter, we keep the other the same as those used in Table I.

The tracking results for different numbers of particles are given in Table II. As expected, in particle filtering, due to the law of large numbers, the larger the number of particles, the less the average tracking error. However, as the number N_{par} of particles increases, more computing resources are required.

TABLE II
TRACKING RESULTS OF PF-SLTR WHEN N_{PAR} VARIES

N_{par}	12	25	50	100	**200**
MSE (unit: m^2)	(Diverged)	0.1116	0.0421	0.0134	**0.0070**
Time (unit: ms)	2.1	3.4	7.4	15.3	**29.2**

Note: Boldfaced values are baselines in Table I.

The tracking results for different transmit SNRs are given in Table III. As indicated, the larger value of the transmit SNR helps decrease the average tracking error. We do not report the running times because the value of the transmit SNR does not essentially affect the computational complexity.

TABLE III
TRACKING RESULTS OF PF-SLTR WHEN SNR_{TX} VARIES

SNR_{tx}	-50	-48	-45	-42	-40
MSE (unit: m^2)	(Diverged)	0.3238	0.0956	0.0591	0.0436
SNR_{tx}	-30	-20	**-10**	0	10
MSE (unit: m^2)	0.0119	0.0077	**0.0070**	0.0065	0.0059

Note: Boldfaced values are baselines in Table I.

The tracking results for different numbers of antennas are given in Table IV. As we can anticipate, the larger the number of antennas, the smaller the average tracking error, and the greater the computational burden.

TABLE IV
TRACKING RESULTS OF PF-SLTR WHEN N_t AND N_r VARY

$N_t = N_r =$	21	22	23	24
MSE (unit: m^2)	(Diverged)	0.0346	0.0338	0.0273
Time (unit: ms)	11.4	12.7	13.2	13.4
$N_t = N_r =$	28	32	48	**64**
MSE (unit: m^2)	0.0236	0.0165	0.0090	**0.0070**
Time (unit: ms)	15.2	16.9	20.0	**29.2**

Note: Boldfaced values are baselines in Table I.

The tracking results for different numbers of subcarriers are given in Table V. It suggests that, given subcarrier spacing, the larger the number of subcarriers (i.e., the larger the

bandwidth), the smaller the average tracking error. However, this performance improvement comes with an increase in computational time.

TABLE V
TRACKING RESULTS OF PF-SLTR WHEN N_c VARIES

N_c	32	48	64	128	**256**
MSE (unit: m^2)	(Diverged)	0.2643	0.0797	0.0236	**0.0070**
Time (unit: ms)	9.8	11.2	12.5	19.2	**29.2**

Note: Boldfaced values are baselines in Table I.

The tracking results for different numbers of pulses are given in Table VI, suggesting that a larger number of pulses leads to a smaller average tracking error. This is because when $N_p \geq 2$, Doppler processing is enabled, and the additional information in the radial-velocity domain can be exploited. However, this performance improvement incurs substantial computational costs. Since using range and DoA information is sufficient to determine a target, reliable tracking can still be achieved even when Doppler processing is disabled.

TABLE VI
TRACKING RESULTS OF PF-SLTR WHEN N_p VARIES

N_p	**1**	2	3	4	5
MSE (unit: m^2)	**0.0070**	0.0063	0.0053	0.0051	0.0047
Time (unit: ms)	**29.2**	64.8	132.3	170.5	193.3

Note: Boldfaced values are baselines in Table I.

The tracking results for different values of ξ in (15) and (33) are given in Table VII. We do not report the running times because the value of ξ does not essentially affect the computational complexity. The results show that the value of ξ, which balances the relative importance of the $\boldsymbol{y}_k$-data-evidence compared to the prior belief [cf. (11)], can potentially further improve the performance of PF-SLTR; see also Theorem 1, as well as the texts below it and Example 2. However, the empirically best value of ξ is problem-specific and to be tuned case by case. For the specific scenario in Fig. 3, we empirically found that $\xi = 6$ works best among tested values.

TABLE VII
TRACKING RESULTS OF PF-SLTR WHEN ξ VARIES

ξ	0.50	0.75	**1**	1.25	1.50
MSE (unit: m^2)	0.0105	0.0096	**0.0070**	0.0059	0.0059
ξ	2.00	4.00	6.00	8.00	10.00
MSE (unit: m^2)	0.0057	0.0036	0.0032	0.0046	0.0052

Note: Boldfaced values are baselines in Table I.

For visualization of Tables II-VII, see Appendix D in the online supplementary materials.

VII. CONCLUSIONS

This article proposes a new particle filtering framework to address core challenges in signal-level target tracking using MIMO multi-carrier pulse-Doppler radar. By adopting an optimization-centric interpretation of Bayes' rule, the proposed method eliminates the need for explicit likelihood models and avoids augmenting nuisance parameters (i.e., complex path gains) into the state vector. Instead, the filtering process is driven by evaluating the data evidence of each hypothesized target state using domain-tailored cost functions. This shift achieves significant performance improvements in both running times and tracking accuracy, relative to conventional approaches. Moreover, the proposed framework is adapted for implementation in MIMO-OFDM systems, enabling practical integration with existing communication infrastructures to realize joint sensing and communication capabilities. Both the pulsed paradigm for tracking far and fast targets and the continuous-wave scheme for tracking near and slow targets are discussed. Simulation results confirm the effectiveness of the proposed approaches in diverse MIMO-OFDM ISAC configurations, demonstrating the real-time feasibility and reliable tracking performance under unknown likelihood models.

REFERENCES

[1] K. V. Mishra, M. B. Shankar, V. Koivunen, B. Ottersten, and S. A. Vorobyov, "Toward millimeter-wave joint radar communications: A signal processing perspective," *IEEE Signal Processing Mag.*, vol. 36, no. 5, pp. 100–114, 2019.

[2] F. Liu, L. Zheng, Y. Cui, C. Masouros, A. P. Petropulu, H. Griffiths, and Y. C. Eldar, "Seventy years of radar and communications: The road from separation to integration," *IEEE Signal Processing Mag.*, vol. 40, no. 5, pp. 106–121, 2023.

[3] F. Liu, W. Yuan, C. Masouros, and J. Yuan, "Radar-assisted predictive beamforming for vehicular links: Communication served by sensing," *IEEE Trans. Wireless Commun.*, vol. 19, no. 11, pp. 7704–7719, 2020.

[4] F. Dong, F. Liu, S. Lu, Y. Xiong, Q. Zhang, Z. Feng, and F. Gao, "Communication-assisted sensing in 6G networks," *IEEE J. Sel. Areas in Commun.*, vol. 43, pp. 1371–1386, 2025.

[5] M. A. Richards, *Fundamentals of Radar Signal Processing*, 3rd ed. McGraw-Hill New York, 2022.

[6] Z. Zhang, L. Chen, J. Xing, K. Liu, and Q. Chang, "Sensing-assisted intelligent transportation system with adaptive power allocation and automatic beam control," *IEEE Trans. Intell. Transp. Syst.*, vol. 26, pp. 8820–8833, 2025.

[7] L. Lu, G. Y. Li, A. L. Swindlehurst, A. Ashikhmin, and R. Zhang, "An overview of massive MIMO: Benefits and challenges," *IEEE J. Sel. Topics Signal Processing*, vol. 8, no. 5, pp. 742–758, 2014.

[8] Y. Li, N. Seshadri, and S. Ariyavisitakul, "Channel estimation for OFDM systems with transmitter diversity in mobile wireless channels," *IEEE J. Sel. Areas in Commun.*, vol. 17, no. 3, pp. 461–471, 1999.

[9] Y. G. Li, J. H. Winters, and N. R. Sollenberger, "MIMO-OFDM for wireless communications: Signal detection with enhanced channel estimation," *IEEE Trans. Commun.*, vol. 50, no. 9, pp. 1471–1477, 2002.

[10] P. Stoica, J. Li, and Y. Xie, "On probing signal design for MIMO radar," *IEEE Trans. Signal Processing*, vol. 55, no. 8, pp. 4151–4161, 2007.

[11] L. Xu, J. Li, and P. Stoica, "Target detection and parameter estimation for MIMO radar systems," *IEEE Trans. Aerosp. Electron. Syst.*, vol. 44, no. 3, pp. 927–939, 2008.

[12] G. Cui, H. Li, and M. Rangaswamy, "MIMO radar waveform design with constant modulus and similarity constraints," *IEEE Trans. Signal Processing*, vol. 62, no. 2, pp. 343–353, 2013.

[13] V. Koivunen, M. F. Keskin, H. Wymeersch, M. Valkama, and N. González-Prelcic, "Multicarrier ISAC: Advances in waveform design, signal processing, and learning under nonidealities," *IEEE Signal Processing Mag.*, vol. 41, no. 5, pp. 17–30, 2024.

[14] Y. Zhang, S. Aditya, and B. Clerckx, "Input distribution optimization in OFDM dual-function radar-communication systems," *IEEE Trans. Signal Processing*, vol. 72, pp. 5258–5273, 2024.

[15] C. Sturm and W. Wiesbeck, "Waveform design and signal processing aspects for fusion of wireless communications and radar sensing," *Proc. IEEE*, vol. 99, no. 7, pp. 1236–1259, 2011.

[16] Z. Xiao, R. Liu, M. Li, Q. Liu, and A. L. Swindlehurst, "A novel joint angle-range-velocity estimation method for MIMO-OFDM ISAC systems," *IEEE Trans. Signal Processing*, vol. 72, pp. 3805–3818, 2024.

[17] M. F. Keskin, H. Wymeersch, and V. Koivunen, "Monostatic sensing with OFDM under phase noise: From mitigation to exploitation," *IEEE Trans. Signal Processing*, vol. 71, pp. 1363–1378, 2023.

[18] S. Mercier, S. Bidon, D. Roque, and C. Enderli, "Comparison of correlation-based OFDM radar receivers," *IEEE Trans. Aerosp. Electron. Syst.*, vol. 56, no. 6, pp. 4796–4813, 2020.

[19] G. San Antonio, D. R. Fuhrmann, and F. C. Robey, "MIMO radar ambiguity functions," *IEEE J. Sel. Topics Signal Processing*, vol. 1, no. 1, pp. 167–177, 2007.

[20] Y. Xiong, F. Liu, Y. Cui, W. Yuan, T. X. Han, and G. Caire, "On the fundamental tradeoff of integrated sensing and communications under Gaussian channels," *IEEE Trans. Inform. Theory*, vol. 69, no. 9, pp. 5723–5751, 2023.

[21] N. R. Olson, J. G. Andrews, and R. W. Heath, "Coverage and rate of joint communication and parameter estimation in wireless networks," *IEEE Trans. Inform. Theory*, vol. 70, no. 1, pp. 206–243, 2023.

[22] M. Ahmadipour, M. Kobayashi, M. Wigger, and G. Caire, "An information-theoretic approach to joint sensing and communication," *IEEE Trans. Inform. Theory*, vol. 70, no. 2, pp. 1124–1146, 2022.

[23] F. Liu, Y. Zhang, Y. Xiong, S. Li, W. Yuan, F. Gao, S. Jin, and G. Caire, "CP-OFDM achieves the lowest average ranging sidelobe under QAM/PSK constellations," *IEEE Trans. Inform. Theory*, vol. 71, pp. 6950–6967, 2025.

[24] C. R. Berger, B. Demissie, J. Heckenbach, P. Willett, and S. Zhou, "Signal processing for passive radar using OFDM waveforms," *IEEE J. Sel. Topics Signal Processing*, vol. 4, no. 1, pp. 226–238, 2010.

[25] L. Zheng and X. Wang, "Super-resolution delay-Doppler estimation for OFDM passive radar," *IEEE Trans. Signal Processing*, vol. 65, no. 9, pp. 2197–2210, 2017.

[26] M. Wu and C. Hao, "Super-resolution TOA and AOA estimation for OFDM radar systems based on compressed sensing," *IEEE Trans. Aerosp. Electron. Syst.*, vol. 58, no. 6, pp. 5730–5740, 2022.

[27] X. Hu, C. Masouros, F. Liu, and R. Nissel, "Low-PAPR DFRC MIMO-OFDM waveform design for integrated sensing and communications," in *ICC 2022-IEEE International Conference on Communications*. IEEE, 2022, pp. 1599–1604.

[28] P. Li, M. Li, R. Liu, Q. Liu, and A. L. Swindlehurst, "MIMO-OFDM ISAC waveform design for range-Doppler sidelobe suppression," *IEEE Trans. Wireless Commun.*, vol. 24, pp. 1001–1015, 2025.

[29] F. Liu, Y.-F. Liu, A. Li, C. Masouros, and Y. C. Eldar, "Cramér-Rao bound optimization for joint radar-communication beamforming," *IEEE Trans. Signal Processing*, vol. 70, pp. 240–253, 2021.

[30] S. Lu, F. Liu, F. Dong, Y. Xiong, J. Xu, Y.-F. Liu, and S. Jin, "Random ISAC signals deserve dedicated precoding," *IEEE Trans. Signal Processing*, vol. 72, pp. 3453–3469, 2024.

[31] Z. Du, F. Liu, Y. Xiong, T. X. Han, Y. C. Eldar, and S. Jin, "Reshaping the ISAC tradeoff under OFDM signaling: A probabilistic constellation shaping approach," *IEEE Trans. Signal Processing*, vol. 72, pp. 4782–4797, 2024.

[32] F. Liu, Y. Xiong, S. Lu, S. Li, W. Yuan, C. Masouros, S. Jin, and G. Caire, "Uncovering the iceberg in the sea: Fundamentals of pulse shaping and modulation design for random ISAC signals," *IEEE Trans. Signal Processing*, vol. 73, pp. 2511–2526, 2025.

[33] T. Xu, F. Liu, C. Masouros, and I. Darwazeh, "An experimental proof of concept for integrated sensing and communications waveform design," *IEEE Open J. Commun. Soc.*, vol. 3, pp. 1643–1655, 2022.

[34] F. Gu, P. Zhu, Y. Jiang, D. Wang, and Y. Wang, "Beam tracking for distributed millimeter-wave MIMO-OFDM systems with unscented particle filter," in *2023 IEEE 23rd International Conference on Communication Technology (ICCT)*. IEEE, 2023, pp. 534–539.

[35] X. R. Li and V. P. Jilkov, "Survey of maneuvering target tracking: Part I. dynamic models," *IEEE Trans. Aerosp. Electron. Syst.*, vol. 39, no. 4, pp. 1333–1364, 2003.

[36] S. Herbert, J. R. Hopgood, and B. Mulgrew, "MMSE adaptive waveform design for active sensing with applications to MIMO radar," *IEEE Trans. Signal Processing*, vol. 66, no. 5, pp. 1361–1373, 2017.

[37] D. Simon, *Optimal State Estimation: Kalman, H-Infinity, and Nonlinear Approaches*. John Wiley & Sons, 2006.

[38] M. S. Arulampalam, S. Maskell, N. Gordon, and T. Clapp, "A tutorial on particle filters for online nonlinear/non-Gaussian Bayesian tracking," *IEEE Trans. Signal Processing*, vol. 50, no. 2, pp. 174–188, 2002.

[39] S. Godsill, "Particle filtering: the first 25 years and beyond," in *ICASSP 2019-2019 IEEE International Conference on Acoustics, Speech and Signal Processing (ICASSP)*. IEEE, 2019, pp. 7760–7764.

[40] P. Ratpunpairoj, W. Kongprawechnon, K. Fukawa, and K. Kaemarungsi, "A particle filter for objects tracking in cognitive MIMO system," in *2015 6th International Conference of Information and Communication Technology for Embedded Systems (IC-ICTES)*. IEEE, 2015, pp. 1–4.

[41] W. Huleihel, J. Tabrikian, and R. Shavit, "Optimal adaptive waveform design for cognitive MIMO radar," *IEEE Trans. Signal Processing*, vol. 61, no. 20, pp. 5075–5089, 2013.

[42] S. Wang, "Distributionally robust state estimation for jump linear systems," *IEEE Trans. Signal Processing*, vol. 71, pp. 3835–3851, 2023.

[43] X. R. Li and V. P. Jilkov, "Survey of maneuvering target tracking: Part III. measurement models," in *Signal and Data Processing of Small Targets 2001*, vol. 4473. SPIE, 2001, pp. 423–446.

[44] L. D. Stone, R. L. Streit, T. L. Corwin, and K. L. Bell, *Bayesian Multiple Target Tracking*, 2nd ed. Artech House, 2014.

[45] S. J. Davey, "SNR limits on Kalman filter detect-then-track," *IEEE Signal Processing Lett.*, vol. 20, no. 8, pp. 767–770, 2013.

[46] S. Herbert, J. R. Hopgood, and B. Mulgrew, "Computationally simple MMSE (A-optimal) adaptive beam-pattern design for MIMO active sensing systems via a linear-Gaussian approximation," *IEEE Trans. Signal Processing*, vol. 66, no. 18, pp. 4935–4945, 2018.

[47] S. J. Davey, M. G. Rutten, and B. Cheung, "A comparison of detection performance for several track-before-detect algorithms," *EURASIP Journal on Advances in Signal Processing*, vol. 2008, pp. 1–10, 2007.

[48] S. J. Davey, M. G. Rutten, and N. J. Gordon, "Track-before-detect techniques," *Integrated Tracking, Classification, and Sensor Management*, pp. 311–362, 2013.

[49] J. A. Zhang, F. Liu, C. Masouros, R. W. Heath, Z. Feng, L. Zheng, and A. Petropulu, "An overview of signal processing techniques for joint communication and radar sensing," *IEEE J. Sel. Topics Signal Processing*, vol. 15, no. 6, pp. 1295–1315, 2021.

[50] A. Doucet, N. De Freitas, N. J. Gordon *et al.*, *Sequential Monte Carlo methods in Practice*. Springer, 2001, vol. 1, no. 2.

[51] C. Snyder, T. Bengtsson, P. Bickel, and J. Anderson, "Obstacles to high-dimensional particle filtering," *Monthly Weather Review*, vol. 136, no. 12, pp. 4629–4640, 2008.

[52] T. Schon, F. Gustafsson, and P.-J. Nordlund, "Marginalized particle filters for mixed linear/nonlinear state-space models," *IEEE Trans. Signal Processing*, vol. 53, no. 7, pp. 2279–2289, 2005.

[53] O. Cappé, S. J. Godsill, and E. Moulines, "An overview of existing methods and recent advances in sequential Monte Carlo," *Proc. IEEE*, vol. 95, no. 5, pp. 899–924, 2007.

[54] P. Germain, F. Bach, A. Lacoste, and S. Lacoste-Julien, "PAC-Bayesian theory meets Bayesian inference," *Advances in Neural Information Processing Systems*, vol. 29, 2016.

[55] P. G. Bissiri, C. C. Holmes, and S. G. Walker, "A general framework for updating belief distributions," *Journal of the Royal Statistical Society Series B: Statistical Methodology*, vol. 78, no. 5, pp. 1103–1130, 2016.

[56] J. Knoblauch, J. Jewson, and T. Damoulas, "An optimization-centric view on Bayes' rule: Reviewing and generalizing variational inference," *Journal of Machine Learning Research*, vol. 23, no. 132, pp. 1–109, 2022.

[57] Y. Baek, W. Aquino, and S. Mukherjee, "Generalized Bayes approach to inverse problems with model misspecification," *Inverse Problems*, vol. 39, no. 10, p. 105011, 2023.

[58] R. Martin and N. Syring, "Direct Gibbs posterior inference on risk minimizers: Construction, concentration, and calibration," in *Handbook of Statistics*. Elsevier, 2022, vol. 47, pp. 1–41.

[59] G. Lellouch, A. Mishra, and M. Inggs, "Processing alternatives in OFDM radar," in *2014 International Radar Conference*. IEEE, 2014, pp. 1–6.

[60] R. W. Heath, N. Gonzalez-Prelcic, S. Rangan, W. Roh, and A. M. Sayeed, "An overview of signal processing techniques for millimeter wave MIMO systems," *IEEE J. Sel. Topics Signal Processing*, vol. 10, no. 3, pp. 436–453, 2016.

[61] M. S. Davis, *MIMO Radar*. SciTech Publishing, Edison, NJ., 2013, ch. Chapter 4, pp. 119–145.

[62] J. Kwon, N. Kwak, E. Yang, and K. Kim, "Particle filter based track-before-detect method in the range-Doppler domain," in *2019 IEEE Radar Conference (RadarConf)*. IEEE, 2019, pp. 1–5.

[63] J. Vermaak, S. J. Godsill, and P. Perez, "Monte Carlo filtering for multi target tracking and data association," *IEEE Trans. Aerosp. Electron. Syst.*, vol. 41, no. 1, pp. 309–332, 2005.

[64] N. Ito and S. Godsill, "A multi-target track-before-detect particle filter using superpositional data in non-Gaussian noise," *IEEE Signal Processing Lett.*, vol. 27, pp. 1075–1079, 2020.

[65] X. Wang, T. Li, S. Sun, and J. M. Corchado, "A survey of recent advances in particle filters and remaining challenges for multitarget tracking," *Sensors*, vol. 17, no. 12, p. 2707, 2017.

[66] A. Conti, S. Mazuelas, S. Bartoletti, W. C. Lindsey, and M. Z. Win, "Soft information for localization-of-things," *Proc. IEEE*, vol. 107, no. 11, pp. 2240–2264, 2019.

Supplementary Materials

Appendix A
Proof of Proposition 1

Proof: Solve (19) with respect to γ, yielding

$$\begin{aligned}\rho_1(\boldsymbol{y},\boldsymbol{\varphi}) &= \sum_{p=0}^{N_p-1}\sum_{l=0}^{L-1}\boldsymbol{y}_p^{\mathsf{H}}(l)\boldsymbol{y}_p(l) - \frac{\left|\sum_{p=0}^{N_p-1}\sum_{l=0}^{L-1}\boldsymbol{y}_p^{\mathsf{H}}(l)\boldsymbol{b}(\theta)\boldsymbol{a}^{\mathsf{H}}(\theta)\boldsymbol{s}_p(l-\tau)e^{j2\pi pT_r\nu}\right|^2}{\sum_{p=0}^{N_p-1}\sum_{l=0}^{L-1}\boldsymbol{a}^{\mathsf{H}}(\theta)\boldsymbol{s}_p(l-\tau)\boldsymbol{s}_p^{\mathsf{H}}(l-\tau)\boldsymbol{a}(\theta)\boldsymbol{b}^{\mathsf{H}}(\theta)\boldsymbol{b}(\theta)} \\ &\geq 0.\end{aligned} \tag{47}$$

The denominator in the second line equals

$$N_rN_p\boldsymbol{a}^{\mathsf{H}}(\theta)\sum_{l=0}^{L_{\text{ss}}-1}\boldsymbol{s}_p(l)\boldsymbol{s}_p^{\mathsf{H}}(l)\boldsymbol{a}(\theta) = N_rN_pL_{\text{ss}}\boldsymbol{a}^{\mathsf{H}}(\theta)\hat{\boldsymbol{R}}_s\boldsymbol{a}(\theta).$$

Note that $L_{\text{ss}} \leq L$ and $\boldsymbol{s}_p(l) = \boldsymbol{0}$ if $L_{\text{ss}} \leq l \leq L-1$, for every $p \in [N_p]$. This completes the proof. □

Appendix B
Proof of Proposition 3

Proof: When scatterers (including targets of non-interest) are well-separated from the ToI, the interference energy due to scatterers, after matched filtering, can be negligible within the specified tracking gate [5], [19], [61]. Hence, it is equivalent to examine the simplified (i.e., scatterer-free) version of the frequency-domain signal model (5):

$$\bar{\mathbf{y}}_p(n) = \beta_0\boldsymbol{b}(\theta_0)\boldsymbol{a}^{\mathsf{H}}(\theta_0)\bar{\mathbf{s}}_p(n)e^{-j2\pi n\Delta\tau_0}e^{j2\pi pT_r\nu_0} + \bar{\mathbf{n}}_p(n),$$

where $\bar{\mathbf{n}}_p(n)$ denotes the pure (i.e., scatterer-free) channel noise; $\bar{\mathbf{n}}_p(n)$ is uncorrelated with $\bar{\mathbf{s}}_p(n)$ for every $n \in [N_{\text{cr}}]$ and $p \in [N_p]$. After matched filtering, we have (48)-(50).

The first nulls of the Dirichlet function, or the periodic sinc function, in (50) is given by the following conditions in each independent dimension: $\frac{N_t}{2}(\sin\theta_0 - \sin\theta) = \pm 1$, $\frac{N_r}{2}(\sin\theta_0 - \sin\theta) = \pm 1$, $B(\tau_0 - \tau) = \pm 1$, and $T_i(\nu - \nu_0) = \pm 1$. Therefore, within the tracking gate

$$\left[\tau_0 - \frac{1}{B}, \tau_0 + \frac{1}{B}\right] \times \left[\nu_0 - \frac{1}{T_i}, \nu_0 + \frac{1}{T_i}\right] \times \left[\arcsin\left(\sin\theta_0 - \frac{2}{N_{tr}}\right), \arcsin\left(\sin\theta_0 + \frac{2}{N_{tr}}\right)\right],$$

the Dirichlet function is nonzero and satisfies Rule 1. This completes the proof. □

Appendix C
Proof of Theorem 1

Proof: We have

$$\begin{aligned}-\sum_{i=0}^{N_{\text{par}}-1}\alpha_i^{(\xi)}\ln\alpha_i^{(\xi)} &= \sum_{i=0}^{N_{\text{par}}-1} -\frac{\alpha_i^\xi}{C_\xi}\ln\frac{\alpha_i^\xi}{C_\xi} = \sum_{i=0}^{N_{\text{par}}-1} -\frac{\alpha_i^\xi}{C_\xi}\ln\alpha_i^\xi + \frac{\alpha_i^\xi}{C_\xi}\ln C_\xi \\ &= \frac{C_\xi\ln C_\xi}{C_\xi} - \frac{\xi}{C_\xi}\sum_{i=0}^{N_{\text{par}}-1}\alpha_i^\xi\ln\alpha_i.\end{aligned}$$

The derivative with respect to ξ is

$$\frac{\xi}{C_\xi^2}\left\{\left[\sum_{i=0}^{N_{\text{par}}-1}\alpha_i^\xi\ln\alpha_i\right]^2 - \left[\sum_{i=0}^{N_{\text{par}}-1}\alpha_i^\xi\right]\left[\sum_{i=0}^{N_{\text{par}}-1}\alpha_i^\xi\ln\alpha_i\ln\alpha_i\right]\right\} \leq 0,$$

where the inequality is due to the Cauchy inequality, and the equality holds if and only if $\boldsymbol{\alpha}$ is a uniform distribution. Therefore, the entropy function $\xi \mapsto -\sum_{i=0}^{N_{\text{par}}-1}\alpha_i^{(\xi)}\ln\alpha_i^{(\xi)}$ is monotonically decreasing in $\xi \geq 0$. □

$$\bar{\mathbf{y}}_p^{\mathsf{H}}(n)\boldsymbol{b}(\theta)\boldsymbol{a}^{\mathsf{H}}(\theta)\bar{\mathbf{s}}_p(n)e^{-j2\pi n\Delta\tau}e^{j2\pi pT_r\nu} = \beta_0^{\mathsf{H}}\boldsymbol{b}^{\mathsf{H}}(\theta)\boldsymbol{b}(\theta_0)\boldsymbol{a}^{\mathsf{H}}(\theta_0)\bar{\mathbf{s}}_p(n)\bar{\mathbf{s}}_p^{\mathsf{H}}(n)\boldsymbol{a}(\theta)e^{j2\pi n\Delta(\tau_0-\tau)}e^{j2\pi pT_r(\nu-\nu_0)} + \bar{\mathbf{n}}_p^{\mathsf{H}}(n)\boldsymbol{b}(\theta)\boldsymbol{a}^{\mathsf{H}}(\theta)\bar{\mathbf{s}}_p(n)e^{-j2\pi n\Delta\tau}e^{j2\pi pT_r\nu} \tag{48}$$

$$\begin{aligned}
&\mathbb{E}_{\{\bar{\mathbf{y}}_p(n),\bar{\mathbf{s}}_p(n)\}_{\forall p,n}}\left\{\sum_{p=0}^{N_p-1}\sum_{n=0}^{N_{\mathrm{cr}}-1}\left[\bar{\mathbf{y}}_p^{\mathsf{H}}(n)\boldsymbol{b}(\theta)\boldsymbol{a}^{\mathsf{H}}(\theta)\bar{\mathbf{s}}_p(n)e^{-j2\pi n\Delta\tau}e^{j2\pi pT_r\nu}\right]\right\}\\
&= \beta_0^{\mathsf{H}}\boldsymbol{b}^{\mathsf{H}}(\theta)\boldsymbol{b}(\theta_0)\boldsymbol{a}^{\mathsf{H}}(\theta_0)\boldsymbol{R}_s\boldsymbol{a}(\theta)\sum_{n=0}^{N_{\mathrm{cr}}-1}e^{j2\pi n\Delta(\tau_0-\tau)}\sum_{p=0}^{N_p-1}e^{j2\pi pT_r(\nu-\nu_0)} +\\
&\qquad \mathbb{E}_{\{\bar{\mathbf{n}}_p(n),\bar{\mathbf{s}}_p(n)\}_{\forall p,n}}\left\{\boldsymbol{a}^{\mathsf{H}}(\theta)\sum_{p=0}^{N_p-1}\sum_{n=0}^{N_{\mathrm{cr}}-1}\bar{\mathbf{s}}_p(n)\bar{\mathbf{n}}_p^{\mathsf{H}}(n)e^{-j2\pi n\Delta\tau}e^{j2\pi pT_r\nu}\boldsymbol{b}(\theta)\right\}\\
&= \beta_0^{\mathsf{H}}P_t\boldsymbol{b}^{\mathsf{H}}(\theta)\boldsymbol{b}(\theta_0)\boldsymbol{a}^{\mathsf{H}}(\theta_0)\boldsymbol{a}(\theta)\sum_{n=0}^{N_{\mathrm{cr}}-1}e^{j2\pi n\Delta(\tau_0-\tau)}\sum_{p=0}^{N_p-1}e^{j2\pi pT_r(\nu-\nu_0)} + 0\\
&= \beta_0^{\mathsf{H}}P_t\sum_{t=0}^{N_t-1}e^{j\pi t(\sin\theta-\sin\theta_0)}\sum_{r=0}^{N_r-1}e^{j\pi r(\sin\theta_0-\sin\theta)}\sum_{n=0}^{N_{\mathrm{cr}}-1}e^{j2\pi n\Delta(\tau_0-\tau)}\sum_{p=0}^{N_p-1}e^{j2\pi pT_r(\nu-\nu_0)}\\
&= \beta_0^{\mathsf{H}}P_t\sum_{t=0}^{N_t-1}e^{j2\pi\frac{t}{N_t}\frac{N_t}{2}(\sin\theta-\sin\theta_0)}\sum_{r=0}^{N_r-1}e^{j2\pi\frac{r}{N_r}\frac{N_r}{2}(\sin\theta_0-\sin\theta)}\sum_{n=0}^{N_{\mathrm{cr}}-1}e^{j2\pi\frac{n}{N_{\mathrm{cr}}}B(\tau_0-\tau)}\sum_{p=0}^{N_p-1}e^{j2\pi\frac{p}{N_p}T_i(\nu-\nu_0)}
\end{aligned} \tag{49}$$

$$\begin{aligned}
\big|(49)\big| = |\beta_0|\cdot P_t\cdot&\left|\frac{\sin[\pi\cdot(\frac{N_t}{2}(\sin\theta-\sin\theta_0))]}{\sin[\pi\cdot(\frac{N_t}{2}(\sin\theta-\sin\theta_0))/N_t]}\right|\cdot\left|\frac{\sin[\pi\cdot(\frac{N_r}{2}(\sin\theta_0-\sin\theta))]}{\sin[\pi\cdot(\frac{N_r}{2}(\sin\theta_0-\sin\theta))/N_r]}\right|\cdot\\
&\left|\frac{\sin[\pi\cdot(B(\tau_0-\tau))]}{\sin[\pi\cdot(B(\tau_0-\tau))/N_{\mathrm{cr}}]}\right|\cdot\left|\frac{\sin[\pi\cdot(T_i(\nu-\nu_0))]}{\sin[\pi\cdot(T_i(\nu-\nu_0))/N_p]}\right|
\end{aligned} \tag{50}$$

APPENDIX D
ADDITIONAL EXPERIMENTAL RESULTS

A. CW MIMO-OFDM Case

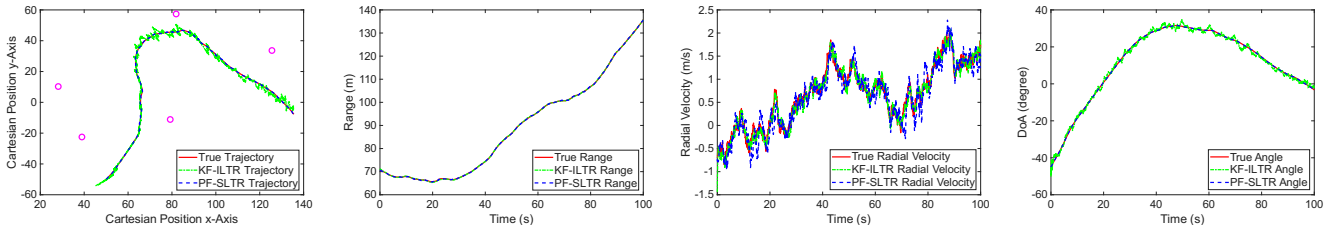
The tracking results of KF-ILTR and PF-SLTR are visually illustrated in Fig. 4. As indicated, PF-SLTR demonstrates a clear advantage over KF-ILTR, especially visible in trajectory and DoA tracking, which agrees with the observations from Table I.

The visualization of Tables II-VII is shown in Fig. 5.

Fig. 6 shows the tracking results of PF-SLTR under the breakdown conditions in Tables II, III, IV, and V, corresponding to $N_{\text{par}} \coloneqq 12$, the transmit SNR $\coloneqq -50$dB, $N_t \coloneqq N_r \coloneqq 21$, and $N_c \coloneqq 32$, respectively. The results suggest that PF-SLTR can initially follow the true trajectory under all four scenarios, but the estimated trajectory eventually deviates from the ground truth. This is because, as the target range increases, the receive SNR quickly decreases due to the range-dependent path loss; see (46). Once the range exceeds a certain threshold, the received echoes become too weak to provide sufficiently reliable measurement information for particle weighting, especially when the number of particles is small. Consequently, the particle set drifts away from the true trajectory, leading to tracking failures.

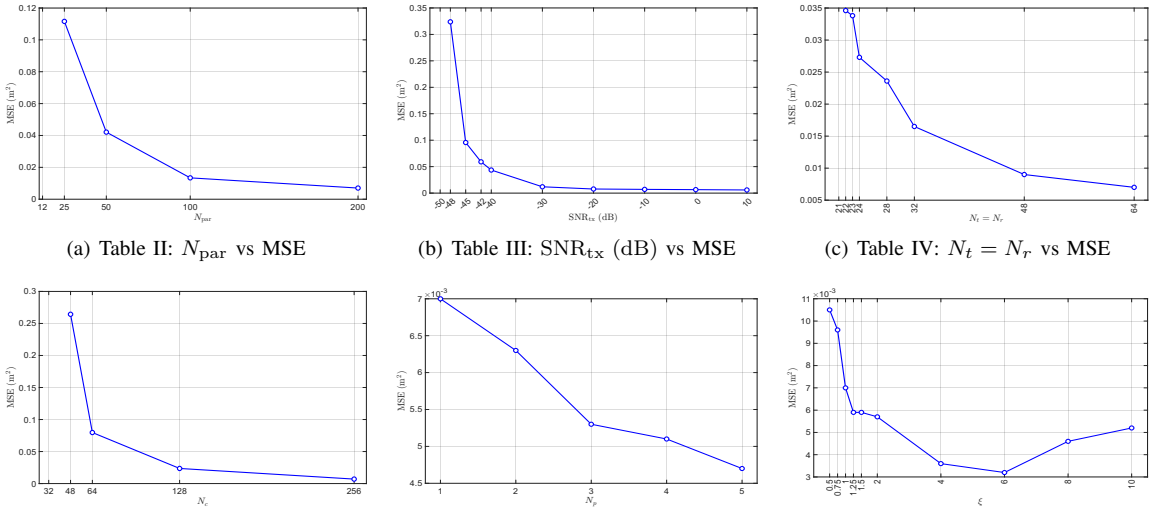
We close this subsection with the following remark on the relation between tracking accuracy and radar resolution.

Remark 1: In the main body of the article, it states that the bandwidth is $B = 51.2$ MHz, so the sampling time interval and the round-trip delay resolution are $T_s = 1/B = 0.019531\mu$s. The corresponding range resolution is therefore $C/(2B) \approx 2.93$m. Moreover, for the 64-element half-wavelength receive array, the resolution in the $\sin$-DoA domain is $2/64 = 1/32$. These resolution values can be used as reference scales for interpreting the tracking results. To be specific, results in Tables II$-$VI are consistent with radar intuition: Larger bandwidth improves range discrimination, larger antenna aperture improves angular discrimination and spatial processing capability, and larger time-on-target improves Doppler discrimination. However, we clarify that tracking accuracy and radar resolution are related but not identical concepts. Radar resolution characterizes the ability to separate two closely spaced targets, whereas the tracking error reported in the experiments measures the estimation accuracy of a single ToI over time. Therefore, when the ToI is sufficiently isolated and temporal filtering is exploited, the tracking RMSE (root-MSE) can be smaller than the nominal range/angle/Doppler resolution, which does not contradict classical radar-resolution theory. □



(a) Trajectory (b) Range (c) Radial Velocity (d) DoA

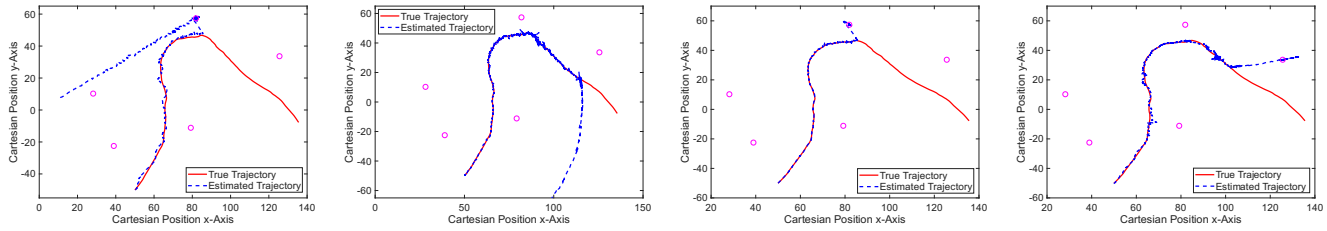
Fig. 4. Tracking results of KF-ILTR and PF-SLTR. Consistent with the results in Table I, PF-SLTR demonstrates a clear advantage over KF-ILTR.



(a) Table II: N_{par} vs MSE (b) Table III: SNR_{tx} (dB) vs MSE (c) Table IV: $N_t = N_r$ vs MSE

(d) Table V: N_c vs MSE (e) Table VI: N_p vs MSE (f) Table VII: ξ vs MSE

Fig. 5. Visualization of the tracking MSEs versus configuration parameters in Tables II-VII.



(a) $N_{\text{par}} = 12$ (b) Transmit SNR = -50dB (c) $N_t = N_r = 21$ (d) $N_c = 32$

Fig. 6. Tracking results of PF-SLTR under breakdown conditions; cf. Tables II, III, IV, and V.

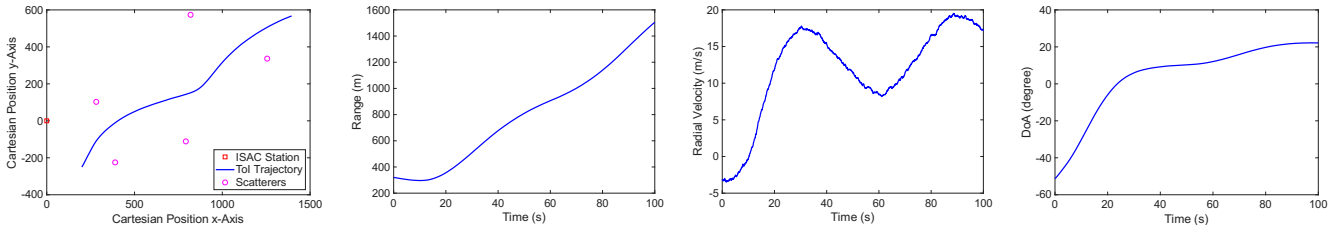
B. Pulsed MIMO-OFDM Case

We consider a pulsed MIMO-OFDM ISAC system with center frequency $f_c = 10$GHz for tracking a *far* and *fast* ToI. The full-duplex working mode is assumed. Unless otherwise stated, all parameter settings remain the same as the continuous-wave case in Fig. 3.

The experimental scenario is displayed in Fig. 7. Therein, the ToI is moving along a curved trajectory, and five static scatterers are assumed, with ranges $[300, 450, 1000, 800, 1300]$ and DoAs $[20, -30, 35, -8, 15]$, respectively. In this case, the ToI and scatterers can be far away from the ISAC station, and the ToI moves quickly; cf. Fig. 3(c) and Fig. 7(c).

We suppose that the pulse repetition interval $T_r := 20\mu$s. Because the pulse length is $T_p = 6\mu$s, as set in the main body of the article, the silent time is 14μs and the duty cycle is $6/20$. Consequently, the maximum detectable round-trip delay is 20μs in the full-duplex mode, corresponding to the maximum detectable distance of 3.0Km. To enable PF-SLTR for the pulsed case, the sensing-centric waveform structure in Fig. 2(b) is used, and the cost function in (27) is employed. Since no data symbols are transmitted during the silent interval, the average communication throughput is reduced by the duty-cycle factor $T_p/T_r = 6/20 = 0.3$.

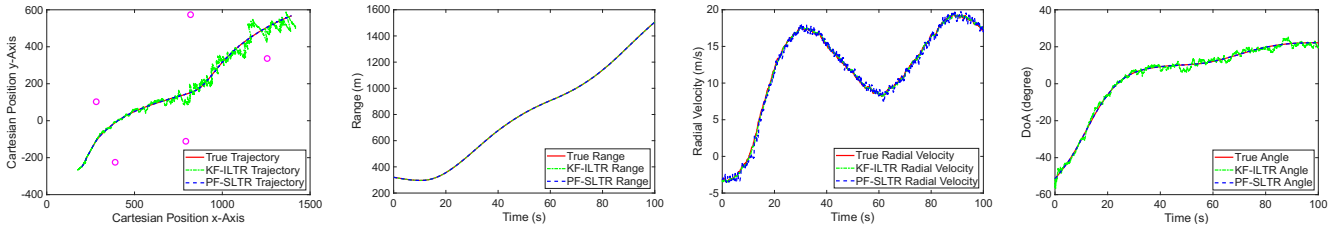
The tracking results of KF-ILTR and PF-SLTR are visually illustrated in Fig. 8. As indicated, PF-SLTR demonstrates a



(a) Trajectory (b) Range (c) Radial Velocity (d) DoA

Fig. 7. Tracking the maneuvering ToI using pulsed MIMO-OFDM ISAC.

clear advantage over KF-ILTR, especially visible in trajectory and DoA tracking. The results associated with PF-SLTR-A and RBPF-SLTR-A are not displayed because they diverge.



(a) Trajectory (b) Range (c) Radial Velocity (d) DoA

Fig. 8. Tracking results of KF-ILTR and PF-SLTR in the pulsed case. As the range increases, the tracking performance deteriorates (particularly visible for KF-ILTR) because the receive SNR decreases rapidly due to range-dependent path loss; see (46).

We do not report other supplementary experimental results for the pulsed case, as they are qualitatively similar to those obtained for the CW case. Interested readers can reproduce the corresponding results (cf. Tables II−VII) using the source code available on GitHub: https://github.com/Spratm-Asleaf/PF-SLTR-MIMO-OFDM.